

Kinetic Simulations of Imbalanced Turbulence in a Relativistic Plasma

Amelia M. Hankla,^{1,2*†} Vladimir Zhdankin,³ Gregory R. Werner,⁴ Dmitri A. Uzdensky⁴
and Mitchell C. Begelman^{1,5}

¹*JILA, University of Colorado and National Institute of Standards and Technology, 440 UCB, Boulder, CO 80309-0440, USA*

²*Department of Physics, University of Colorado, 390 UCB, Boulder, CO 80309-0390, USA*

³*Department of Astrophysical Sciences, Princeton University, 4 Ivy Lane, Princeton, NJ 08544, USA*

⁴*Center for Integrated Plasma Studies, Department of Physics, University of Colorado, 390 UCB, Boulder, CO 80309-0390, USA*

⁵*Department of Astrophysical and Planetary Sciences, University of Colorado, 391 UCB, Boulder, CO 80309, USA*

Last updated 1 September 2021; in original form 1 September 2021

ABSTRACT

Turbulent high-energy astrophysical systems often feature asymmetric energy injection or driving: for instance, nonlinear interactions between Alfvén waves propagating from an accretion disk into its corona. Such systems—relativistic analogs of the solar wind—are “imbalanced”: the energy fluxes parallel and anti-parallel to the large-scale magnetic field are unequal and the plasma therefore possesses net cross-helicity. In the past, numerical studies of imbalanced turbulence have focused on the magnetohydrodynamic regime. In the present study, we investigate externally-driven imbalanced turbulence in a collisionless, ultrarelativistically hot, magnetized pair plasma using three-dimensional particle-in-cell simulations. We find that a turbulent cascade forms for every value of imbalance covered by the simulations and that injected Poynting flux efficiently converts into net momentum of the plasma, a relativistic effect with implications for the launching of a disk wind. Surprisingly, particle acceleration remains efficient even for very imbalanced turbulence. These results characterize properties of imbalanced turbulence in a collisionless plasma and have ramifications for black hole accretion disk coronae, winds, and jets.

Key words: turbulence – plasmas – acceleration of particles – relativistic processes

1 INTRODUCTION

High-energy astrophysical systems often comprise turbulent, collisionless, and relativistically hot plasmas. Turbulence occurs in relativistic active galactic nuclei (AGN) jets and pulsar wind nebulae, as evidenced by high-resolution, multi-wavelength observations (Sparks et al. 1996; Hester 2008), and enables the efficient transport of angular momentum by accretion disks (Shakura & Sunyaev 1973; Balbus & Hawley 1998). Jets, pulsar wind nebulae, and stellar-mass black hole X-ray binary systems (in particular in the steep power-law state) all exhibit power-law radiation spectra extending to very high energies (Remillard & McClintock 2006; Abdo et al. 2009; Aleksić et al. 2015). These power laws are likely the result of synchrotron emission or inverse Compton scattering of ambient photons by a power-law distribution of high-energy electrons (Begelman et al. 1984; Meyer et al. 2010).

Power-law distributions of high-energy particles can be formed through a variety of mechanisms, including turbulence (Kulsrud & Ferrari 1971), magnetic reconnection (Hoshino & Lyubarsky 2012), and collisionless shocks (Blandford & Eichler 1987). All of these mechanisms have successfully produced nonthermal particle acceleration (NTPA) in ab-initio particle-in-cell (PIC) simulations of pulsar wind nebulae (Cerutti et al. 2013), kink-unstable jets (Alves et al. 2018; Davelaar et al. 2020), and the magnetorotational turbulence in

accretion disks (Riquelme et al. 2012; Hoshino 2013). In particular, turbulence efficiently accelerates particles in relativistic, collisionless plasmas with magnetization (the ratio of magnetic enthalpy to plasma enthalpy) $\sigma \gtrsim 1$, as recently demonstrated in PIC simulations (Zhdankin et al. 2017, 2018b; Comisso & Sironi 2018, 2019). For high-energy particles, this turbulent NTPA can be modeled with an advection-diffusion equation in energy space (Schlickeiser 1989; Wong et al. 2020; Demidem et al. 2020; Lemoine 2021). Though NTPA is driven by kinetic processes, many previous analytical and numerical models of high-energy astrophysical systems have treated the plasma as a fluid, employing the framework of magnetohydrodynamics (MHD).

Canonical phenomenological models understand strong MHD turbulence by considering ensembles of counter-propagating Alfvén waves along a background magnetic field (Iroshnikov 1964; Kraichnan 1965; Goldreich & Sridhar 1995; Thompson & Blaes 1998; Boldyrev 2006); see Schekochihin (2020) for a recent review. The nonlinear interaction of these Alfvén waves causes wave packets to deform and cascade to smaller scales over a time-scale assumed to be comparable to the Alfvén time, the time for information to travel at the Alfvén speed along a wave packet in the direction parallel to the background magnetic field (Goldreich & Sridhar 1995). Classic, standard models of MHD turbulence assume that the fluxes of Alfvén waves traveling in opposite directions (parallel vs. anti-parallel to the magnetic field) are equal, or “balanced”. This natural assumption is emphatically not true in a variety of space and astrophysical systems where turbulence is preferentially stirred on one side of the

* E-mail: lia.hankla@gmail.com, amelia.hankla@colorado.edu

† National Science Foundation Graduate Research Fellow

system. For instance, the high temperature of the open-field solar corona might be explained by Alfvén waves generated at the sun’s photosphere that propagate away from the sun and subsequently deposit energy into the corona (Cranmer et al. 2007). Similarly, in an accretion disk-wind system, turbulence in the disk may shake the footpoint of an open large-scale magnetic field line, sending Alfvén waves predominately away from the disk’s midplane and into the corona (Chandran et al. 2018). Such “imbalanced” turbulence possesses net cross-helicity—the difference between the parallel- and anti-parallel-propagating waves’ energies—and has been measured in the solar wind, where phenomenological models have not yet explained the dependence of solar wind’s turbulent energy spectral power-law index on quantities such as cross-helicity (Chen 2016). Beyond the solar system, imbalanced turbulence likely describes many astrophysical systems with asymmetric energy injection. More generally, studying imbalanced turbulence could lead to better understanding of globally balanced turbulence, which comprises local patches of imbalanced turbulence (Perez & Boldyrev 2009).

Studying imbalanced turbulence involves removing the assumption of equal Alfvénic fluxes along the background magnetic field. In the past decade and a half, such studies have focused on the MHD regime, where the subtleties of lifting the previous degeneracy of timescales for counter-propagating waves have fueled phenomenological debates (Lithwick et al. 2007; Chandran 2008; Beresnyak & Lazarian 2008; Perez & Boldyrev 2009). Recent semi-analytical and phenomenological models of imbalanced kinetic turbulence in the nonrelativistic regime have been formulated for scales below the ion Larmor radius (Voitenko & De Keyser 2016; Passot & Sulem 2019; Gogoberidze & Voitenko 2020). Numerical attempts to model imbalanced turbulence in the MHD regime have proven difficult due to questions about the effects of varying dissipation prescriptions, limited dynamic ranges of accessible simulation domains, and limited run times (Beresnyak & Lazarian 2009, 2010; Perez & Boldyrev 2010b,a; Perez et al. 2012; Mason et al. 2012). Some studies have extended beyond standard MHD to the relativistic MHD regime $\sigma \gg 1$ (Cho & Lazarian 2014; Kim & Cho 2015), made approximations of large ion-to-electron mass ratio to model scales below the proton gyroradius (Cho & Kim 2016) or to capture finite Larmor radius effects (Meyrand et al. 2020), or employed a diffusive model to study turbulence from fluid to sub-ion scales (Miloshevich et al. 2020). However, few numerical studies have modeled the fully kinetic collisionless regime—those with an eye towards the solar wind (Grošelj et al. 2018)—and none to our knowledge have examined the ultrarelativistic, collisionless regime relevant to high-energy astrophysical systems. By simulating the fully-kinetic system, we model dissipation self-consistently, avoiding the prescription-dependent problems present in MHD simulations. Exploring this regime is important because quasi-linear models of turbulent particle acceleration for imbalanced MHD predict a decrease in the momentum diffusion coefficient for increasing imbalance, leading to less efficient NTPA and posing a potential obstacle to turbulence as an astrophysical particle accelerator in some systems (Schlickeiser 1989; Chandran 2000).

In this work, we explore the intersection of imbalanced turbulence and relativistic turbulence in magnetized collisionless electron-positron pair plasmas. We use the PIC method in 3D as in Zhankin et al. (2018a) to study how imbalance affects properties of turbulence—including self-consistent NTPA, which is inaccessible in fluid-based models. As a first step, this paper focuses on characterizing the global partition of energy into electromagnetic, internal, turbulent kinetic, and bulk kinetic energy of net motion along the background magnetic field. The internal energy is furthermore

divided into the thermal and nonthermal components. Though the regime we simulate is particularly applicable to black hole accretion disk coronal heating (Chandran et al. 2018) and wind-launching, our results should be generally applicable to relativistic astrophysical turbulence where the source of perturbations is localized, such as the jets originating from AGN.

To frame our study of this numerically- and analytically-unexplored regime of turbulence, we focus on three main questions:

- (i) How does imbalance affect the formation of a turbulent cascade?
- (ii) How does imbalance affect the conversion of energy injected at large scales into electromagnetic energy, internal energy, turbulent kinetic energy and net motion?
- (iii) How does imbalance affect NTPA?

In the following, we characterize global properties of collisionless imbalanced turbulence. We first introduce the numerical tools and parameters used to describe imbalanced turbulence (Section 2). We then present the results of 3D collisionless, relativistic PIC simulations with varying degrees of imbalance and ratio of system size to initial Larmor radius that address each of the above questions in order (Section 3). We conclude by discussing implications for high-energy astrophysical systems and remaining questions (Section 4).

2 METHODS

In this section, we will first review physical properties of relativistic magnetized plasmas (Section 2.1), and then outline the simulation suite used to study imbalanced turbulence (Section 2.2). The last subsection discusses various diagnostics that will be used to analyze our simulations (Section 2.3).

2.1 Plasma Physical Regime

The plasmas considered in this paper are collisionless, ultrarelativistically hot, and magnetized. This section discusses the parameters that characterize such a plasma. Throughout this work, we will use $\langle \cdot \rangle$ to denote the time-dependent volume- or particle ensemble-average of a quantity and $\bar{\cdot}$ to denote the time-average of a quantity in the time interval $10 < tc/L < 20$ unless otherwise specified; here L/c is the light-crossing time of the simulation domain with length L .

An ultra-relativistic, magnetized pair plasma with $\langle \gamma \rangle \gg 1$ has a number of parameters that characterize its properties: an average total (electron plus positron) particle density n_0 , average particle energy $\langle \gamma \rangle m_e c^2$, and characteristic magnetic field strength $B_{\text{rms}} = \sqrt{\langle B_x^2 + B_y^2 + B_z^2 \rangle}$. Here, m_e is the mass of the electron (or positron) and $\langle \gamma \rangle$ is the average particle Lorentz factor ($\gamma = 1/\sqrt{1 - v^2/c^2} = \sqrt{1 + p^2/m_e^2 c^2}$ for a particle with velocity v , mass m_e , and momentum p). The fundamental physical length scales in this plasma are: the characteristic Larmor radius $\rho_e = \langle \gamma \rangle m_e c^2 / e B_{\text{rms}}$, the plasma skin depth $d_e = \left(\langle \gamma \rangle m_e c^2 / (4\pi n_0 e^2) \right)^{1/2}$, and the size of the system L . For a plasma with a Maxwell-Jüttner particle distribution $f(\gamma) = \gamma^2 \sqrt{1 - 1/\gamma^2} [\theta K_2(1/\theta)]^{-1} \exp(-\gamma/\theta)$, the plasma has a well-defined temperature $T_e = \langle \gamma \rangle m_e c^2 / 3$ (assumed equal for electrons and positrons) and the Debye length simplifies to $\lambda_D = d_e / \sqrt{3}$. Here $\theta \equiv kT_e / m_e c^2$ and $K_2(x)$ is the modified Bessel function of the second kind. The three length scales ρ_e , d_e , and L form two dimensionless quantities: the magnetization $\sigma = B_{\text{rms}}^2 / 4\pi h = 3(d_e / \rho_e)^2 / 4$ and the ratio of the largest

characteristic scale of spatial variation $L/2\pi$ (which will be the turbulence driving scale in our study as described below) to the Larmor radius ρ_e . Here $h = n_0 \langle \gamma \rangle m_e c^2 + \langle P \rangle \approx 4n_0 \langle \gamma \rangle m_e c^2 / 3$ is the characteristic relativistic enthalpy density and $\langle P \rangle \approx n_0 \langle \gamma \rangle m_e c^2 / 3$ is the (assumed isotropic) average plasma pressure. The magnetization is related to the plasma beta parameter $\beta = 8\pi \langle P \rangle / B_{\text{rms}}^2$ as $\beta = 1/(2\sigma)$ and determines the relativistic Alfvén speed $v_A = c\sqrt{\sigma/(\sigma+1)}$. Since we consider primarily Alfvénic turbulence, the magnetization governs how relativistic the large-scale turbulent motion is.

2.2 Numerical Simulations

To explore the properties of imbalanced turbulence in a collisionless relativistic pair plasma from first principles, we use the electromagnetic PIC code ZELTRON (Cerutti et al. 2013). ZELTRON samples the particle phase space with macro-particles and evolves them according to the Lorentz force law, providing an approximate solution to the relativistic Vlasov equation. The electric and magnetic fields evolve according to Maxwell’s equations, with the addition of an externally-driven volumetric current to Ampère’s law to generate turbulence, as discussed below.

The physical parameters of the simulations we present are identical to those described in Zhankin et al. (2018a) and Zhankin et al. (2018b) except for the modifications outlined below to introduce imbalance. Each simulation is initialized with an electron-positron plasma at rest with a Maxwell-Jüttner distribution function, a uniform background magnetic field $\mathbf{B}_0 = B_0 \hat{z}$ and no initial electromagnetic fluctuations. For each of the simulations, we set the initial magnetization to $\sigma_0 = 0.5$, yielding a relativistic Alfvén velocity $v_{A0} = 0.58c$ and plasma beta $\beta_0 = 1.0$. The initial temperature of the plasma is fixed at $T_e = 100m_e c^2$ across all simulations, corresponding to an initial average particle Lorentz factor of $\langle \gamma \rangle \approx 300$.

To obtain the largest possible inertial range, the simulation suite’s chosen numerical parameters maximize the separation between the large driving scale $L/2\pi$ and the small initial kinetic scales ρ_{e0} and d_{e0} , while still resolving the latter. We resolve the initial plasma length scales with fixed $\Delta x = \rho_{e0}/1.5 = d_{e0}/1.22$, where $\Delta x = \Delta y = \Delta z$ is the grid cell length in each direction. The simulation domain is cubic with periodic boundary conditions and length $L \equiv N\Delta x$, where N is the number of cells in a spatial dimension (throughout, $N_x = N_y = N_z \equiv N$). The timestep is a fraction of the cell light-crossing time, i.e. $\Delta t = 3^{-1/2}\Delta x/c$. The simulations are initialized with 32 particles per cell per species. To scan the ratio $L/2\pi\rho_{e0}$, we vary the number of cells in each spatial dimension, with $N = 256, 384, 512$, and 768 corresponding to $L/2\pi\rho_{e0} \in \{27.1, 40.7, 54.3, 81.5\}$. When examining the dependence of results on simulation size, we also include three simulations of balanced turbulence with $L/2\pi\rho_{e0} \in \{81.5, 108.7, 164\}$ ($N \in \{768, 1024, 1536\}$) used in Zhankin et al. (2018b) that are otherwise identical to the simulations presented in this work.

The initial equilibrium is disrupted by an externally-driven current. We employ an oscillating Langevin antenna (TenBarge et al. 2014, OLA) to drive turbulence volumetrically and continually throughout each simulation’s duration. The OLA is implemented by adding the external current to the evolution equation for the electric field (Ampère’s law). This current generates counter-propagating Alfvén waves. The amplitudes of these counter-propagating waves are modified to induce imbalanced turbulence, as described in the following paragraphs. Because of the random nature of the OLA driving, a single simulation may not be representative of the entire ensemble of possible random seeds. To avoid basing all our conclusions on a sin-

gle data point for each balance parameter, we also present a statistical study of random seeds. For each balance parameter, eight values of the random seed are simulated for the domain size $L/2\pi\rho_{e0} = 40.7$ ($N = 384$). The results of the statistical study are compared against the largest simulation domains $L/2\pi\rho_{e0} = 81.5$ ($N = 768$) to provide a sense for the statistical variation of each quantity. Statistical variation could potentially be reduced in a single simulation by introducing more than eight driving modes.

We drive imbalanced turbulence via eight independently-evolved, externally-driven sinusoidal current modes. These current modes create magnetic field perturbations propagating in opposite directions along the background magnetic field, i.e. Alfvén waves. The driven current modes have the form:

$$J_x^{\text{ext}}(\mathbf{x}, t) = \frac{2\pi c}{L^2} \text{Re} \left[\sum_{j=1}^2 \left(a_j(t) e^{i\mathbf{k}_j \cdot \mathbf{x}} + b_j(t) e^{-i\mathbf{k}_j \cdot \mathbf{x}} \right) \right] \quad (1)$$

$$J_y^{\text{ext}}(\mathbf{x}, t) = \frac{2\pi c}{L^2} \text{Re} \left[\sum_{j=3}^4 \left(a_j(t) e^{i\mathbf{k}_j \cdot \mathbf{x}} + b_j(t) e^{-i\mathbf{k}_j \cdot \mathbf{x}} \right) \right] \quad (2)$$

$$J_z^{\text{ext}}(\mathbf{x}, t) = \frac{2\pi c}{L^2} \text{Re} \left[\sum_{j=1}^4 \left(-a_j(t) e^{i\mathbf{k}_j \cdot \mathbf{x}} + b_j(t) e^{-i\mathbf{k}_j \cdot \mathbf{x}} \right) \right]. \quad (3)$$

The sign of k_z dictates the direction of the current wave’s propagation. Four of the modes have no y -component of their wavevector and four have no x -component; four propagate in the $+z$ -direction and four propagate in the $-z$ -direction. These wavevectors are

$$\mathbf{k}_1 = k_0(-1, 0, 1) \quad \mathbf{k}_2 = k_0(1, 0, 1) \quad (4)$$

$$\mathbf{k}_3 = k_0(0, -1, 1) \quad \mathbf{k}_4 = k_0(0, 1, 1). \quad (5)$$

Here, $k_0 = 2\pi/L$, so that the driving scale is the largest scale $L/2\pi$. We ensure $\nabla \cdot \mathbf{J}_{\text{ext}} = 0$ to avoid local injection of net charge. Current waves driven in $J_{\text{ext},x}$ and $J_{\text{ext},y}$ create Alfvén waves with magnetic field perturbations in the y - and x -directions, respectively. The amplitudes of these current waves can be adjusted to create counter-propagating Alfvén waves of unequal amplitudes, thus enabling our study of imbalanced turbulence.

The external current’s time-dependence is dictated by the coefficients $a_j(t)$ and $b_j(t)$. The coefficient at the $(n+1)$ th timestep is found from the previous n th timestep as

$$a_j^{(n+1)} = a_j^{(n)} e^{-i\omega\Delta t} + \alpha_j u_j^{(n)} \Delta t \quad (6)$$

$$b_j^{(n+1)} = b_j^{(n)} e^{-i\omega\Delta t} + \beta_j v_j^{(n)} \Delta t. \quad (7)$$

The coefficients $a_j(t)$ and $b_j(t)$ thus oscillate at frequency ω with random kicks at each timestep (cf. Langevin equation, hence the name “oscillating Langevin antenna”; TenBarge et al. 2014). The initial coefficients $a_j^{(0)}$ and $b_j^{(0)}$ are set to amplitudes \mathcal{A} and \mathcal{B} multiplied by random phases $\phi_j^{(a)}$ and $\phi_j^{(b)}$: $a_j^{(0)} = \mathcal{A} e^{i\phi_j^{(a)}}$ and $b_j^{(0)} = \mathcal{B} e^{i\phi_j^{(b)}}$. We set $\mathcal{A} = B_0 L / 8\pi$, which for balanced turbulence achieves $\delta B_{\text{rms}} = \sqrt{B_{\text{rms}}^2 - B_0^2} \sim B_0$. The random kicks $u_j^{(n)}$

and $v_j^{(n)}$ in Equations 6 and 7 are complex random numbers with real and imaginary components drawn from a uniform distribution between -0.5 and 0.5 . The constant parameters α_j and β_j are set such that when ensemble-averaged, $\langle |a_j^{(n)}|^2 \rangle = \mathcal{A}^2$ and $\langle |b_j^{(n)}|^2 \rangle = \mathcal{B}^2$. The complex driving frequency ω has real component ω_0 and an imaginary component $-\Gamma_0$ which we set to be non-integer multiples of the Alfvén frequency $\omega_A \equiv 2\pi v_A / L$ to avoid initial resonances: $\omega_0 = (0.6/\sqrt{3})\omega_A \approx 0.35\omega_A$ and $\Gamma_0 = (0.5/\sqrt{3})\omega_A \approx$

$0.29\omega_A$. In frequency space, the driving is a Lorentzian centered at ω_0 with a full-width half-max of Γ_0 ; see [TenBarge et al. \(2014\)](#) for details. The amplitudes \mathcal{A} and \mathcal{B} (and therefore the α_j and β_j values) are the same for all a_j and b_j , but the random parameters u_j, v_j , and the initial phases $\phi_j^{(a,b)}$ are different for each k_j .

We introduce imbalance by adjusting the amplitudes of the current waves propagating in the $-z$ -direction relative to those propagating in the $+z$ -direction. The coefficients a_j control the current waves propagating in the $+z$ -direction, whereas b_j control the waves propagating in the $-z$ -direction. These current waves' amplitudes are dictated by their respective \mathcal{A} and \mathcal{B} amplitudes. To achieve imbalanced turbulence, we hold \mathcal{A} fixed and vary \mathcal{B} . We quantify how balanced the turbulence is via the *balance parameter*,

$$\xi \equiv \mathcal{B}/\mathcal{A}, \quad (8)$$

where \mathcal{B} is the amplitude for the $-z$ -modes and \mathcal{A} is the fixed amplitude for the $+z$ -modes. A value of $\xi = 1$ corresponds to the canonical balanced case, whereas $\xi = 0$ corresponds to current waves propagating only in the $+z$ -direction. Because we drive current waves rather than Alfvén modes, we do not directly control the exact amplitude of counter-propagating Alfvén waves. If $\xi = 0$ corresponded exactly to the case of Alfvén waves propagating in a single direction, we would not expect turbulence to develop in a non-relativistic, ideal MHD plasma. Indeed, turning off the random kicks by setting $\alpha_j = \beta_j = 0$ does not result in turbulence for simulations with $\xi = 0$ (not shown). However, with our set-up of nonzero α_j and β_j , the $\xi = 0$ case does become turbulent because the OLA forcing excites counter-propagating Alfvén waves. In principle, more imbalanced turbulence should be achievable by, e.g., a decaying turbulence problem. For the present work, we simply term the $\xi = 0$ case the “extremally-imbalanced” case to emphasize that this ξ value is the most imbalanced turbulence that our driving mechanism can achieve.

We will use the balance parameter ξ throughout this paper to refer to the degree of imbalance; however, since ξ is not a standard method of measuring imbalance, we now briefly discuss the relationship of ξ to other methods of measuring imbalance. Cross-helicity, an invariant in ideal MHD, measures the difference in the energy densities associated with waves propagating anti-parallel (with energy density \mathcal{E}_+ and amplitude δB_+) and parallel to the magnetic field (with energy density \mathcal{E}_- and amplitude δB_-). In ideal, non-relativistic, incompressible MHD, $\mathcal{E}_\pm = \langle \rho |z_\pm|^2 \rangle / 4$, where $z_\pm = \delta \mathbf{v} \pm \mathbf{b}$ are the Elsasser variables ([Perez & Boldyrev 2009](#)). Here $\delta \mathbf{v}$ is the fluctuating plasma velocity, $\mathbf{b} \equiv \delta \mathbf{B} v_A / B_0$ is the fluctuating magnetic field in velocity units, and ρ is the plasma mass density (not to be confused with the Larmor radius ρ_e). The total energy density is then given by $\mathcal{E} \equiv \mathcal{E}_+ + \mathcal{E}_- = (1/2) \langle \rho (|\delta \mathbf{v}|^2 + |\mathbf{b}|^2) \rangle$ and the cross-helicity $H_c \equiv (\mathcal{E}_+ - \mathcal{E}_-) / \langle \rho \rangle$ can be re-expressed as $H_c = \langle \delta \mathbf{v} \cdot \mathbf{b} \rangle$. Cross-helicity is related to the volume-averaged z -component of the Poynting flux $\mathcal{S}(\mathbf{x}, t) = (c/4\pi) [\mathbf{E} \times \mathbf{B}]$ under the assumptions of incompressible, nonrelativistic, ideal reduced MHD that $\delta B \ll B_0$ and that the fluctuations $\delta \mathbf{B}$ and $\delta \mathbf{v}$ are perpendicular to the background field $B_0 \hat{z}$:

$$\langle S_z \rangle(t) = -\frac{B_0}{4\pi} \langle \delta \mathbf{v} \cdot \delta \mathbf{B} \rangle = -\frac{1}{4\pi} \frac{B_0^2}{v_A} H_c(t). \quad (9)$$

For a single Alfvén wave, $\delta \mathbf{v} / v_A = \pm \delta \mathbf{B} / B_0$ and thus the magnitude of the Poynting flux for a single Alfvén wave $|\langle S_z \rangle_{1\text{-wave}}|$ is

$$|\langle S_z \rangle_{1\text{-wave}}| = \frac{1}{4\pi} \langle \delta B^2 \rangle v_A. \quad (10)$$

We can estimate the values of the driven Alfvén wave energies in

our simulations of imbalanced turbulence as $E_+ \sim \langle \delta B_+^2 \rangle \sim |a_j|^2$ (where δB_+ is the amplitude of the magnetic perturbation travelling in the $+z$ direction) and $E_- \sim |b_j|^2$, leading to

$$\langle S_z \rangle \propto H_c \propto 1 - \xi^2. \quad (11)$$

Equation 11 will be tested in Section 3.2.4. Normalizing to the total energy, the “normalized cross-helicity” $\tilde{H}_c = (\mathcal{E}_+ - \mathcal{E}_-) / (\mathcal{E}_+ + \mathcal{E}_-)$ ([Perez & Boldyrev 2009](#); [Chen 2016](#); [Meyrand et al. 2020](#)) can be estimated as $\tilde{H}_c \sim (1 - \xi^2) / (1 + \xi^2)$. Another common measurement of imbalance in MHD, the ratio of the energies in the counter-propagating waves $\mathcal{E}_+ / \mathcal{E}_-$ ([Beresnyak & Lazarian 2008](#)), scales as $\mathcal{E}_+ / \mathcal{E}_- \sim \mathcal{A}^2 / \mathcal{B}^2 = 1 / \xi^2$.

The main goal of our study is to determine the impact of imbalance on the properties of collisionless turbulence. We do so by varying the balance parameter ξ between 0 (“extremally-imbalanced”) and 1 (“balanced”) at every value of $L/2\pi\rho_e 0$.

2.3 Energy Diagnostics

In this section, we discuss diagnostics that will be used in Section 3 to partition the energy of the system into four main types.

The total energy density in the system can be decomposed into the energy density \mathcal{E}_{EM} in the electric and magnetic fields and the total (kinetic plus rest mass) energy density \mathcal{E}_{pl} in the plasma particles. Fluid quantities are useful to gain intuition into the plasma’s behavior and to partition \mathcal{E}_{pl} of the plasma particles into internal, net flow, and turbulent flows:

$$\mathcal{E}_{pl}(\mathbf{x}, t) = \mathcal{E}_{int}(\mathbf{x}, t) + \mathcal{E}_{net}(t) + \mathcal{E}_{turb}(\mathbf{x}, t). \quad (12)$$

The plasma’s total kinetic, internal, and turbulent kinetic energy densities are calculated for each simulation cell from both the electron and positron macro-particles’ positions and momenta, though they will often be discussed in terms of their volume averages $\langle \mathcal{E}_{pl} \rangle$, $\langle \mathcal{E}_{int} \rangle$ and $\langle \mathcal{E}_{turb} \rangle$, respectively. The net flow energy density \mathcal{E}_{net} is a key quantity for characterizing how efficiently imbalanced turbulence can drive a directed plasma flow. It is a global quantity calculated from the total momentum in the system. Explicitly, these quantities are defined as:

$$\mathcal{E}_{int}(\mathbf{x}, t) \equiv \sqrt{\mathcal{E}_{pl}^2(\mathbf{x}, t) - \mathcal{P}_{pl}^2(\mathbf{x}, t)c^2} \quad (13)$$

$$\mathcal{E}_{net}(t) \equiv \langle \mathcal{E}_{pl} \rangle(t) - \sqrt{\langle \mathcal{E}_{pl} \rangle^2(t) - \langle \mathcal{P}_{pl} \rangle^2(t)c^2} \quad (14)$$

$$\mathcal{E}_{turb}(\mathbf{x}, t) \equiv \mathcal{E}_{flow}(\mathbf{x}, t) - \mathcal{E}_{net}(t) \quad (15)$$

where $\mathcal{E}_{flow}(\mathbf{x}, t) = \mathcal{E}_{pl}(\mathbf{x}, t) - \mathcal{E}_{int}(\mathbf{x}, t)$ ([Zhdankin et al. 2018a](#), Eq. 8) and $\mathcal{P}_{pl}(\mathbf{x}, t)$ is the local momentum density of the electron-positron plasma. This framework is similar to that in [Zhdankin et al. \(2018a\)](#), with the renaming of the “bulk” energy density to the “flow” kinetic energy density and further breakdown of the flow energy density into the energy density associated with the net flow of the plasma \mathcal{E}_{net} through the simulation domain and the turbulent motions \mathcal{E}_{turb} . Equation 13 for the internal energy density is analogous to the relativistic energy E of a single particle $E^2 = (mc^2)^2 + p^2c^2$. In this analogy, the plasma internal energy acts like a particle rest mass, the plasma momentum acts as a particle momentum, and the total plasma kinetic energy acts like a relativistic particle mass. Equation 14 for the net flow energy density uses a similar analogy, specifically applied to the quantity volume-averages.

The change in the energy of the plasma and the electromagnetic fields comes from the energy injected into the system by the OLA driving. The energy injection rate $\langle \dot{\mathcal{E}}_{inj} \rangle = -\langle \mathbf{J}_{ext} \cdot \mathbf{E} \rangle$ is statistically constant in time. Integrating it over time gives the total injected

energy density up to time t : $\mathcal{E}_{\text{inj}}(t)$. Because the injected energy depends on the amplitude of the driven waves, its value at any given time varies with ξ within a factor of two or so (see Section 3.2). To account for this dependence of injected energy on balance parameter, we normalize the volume-averaged changes in the various energy components by the volume-averaged injected energy to obtain energy efficiencies:

$$1 = \frac{\Delta\langle\mathcal{E}_{\text{int}}\rangle}{\langle\mathcal{E}_{\text{inj}}\rangle} + \frac{\Delta\mathcal{E}_{\text{net}}}{\langle\mathcal{E}_{\text{inj}}\rangle} + \frac{\Delta\langle\mathcal{E}_{\text{turb}}\rangle}{\langle\mathcal{E}_{\text{inj}}\rangle} + \frac{\Delta\langle\mathcal{E}_{\text{EM}}\rangle}{\langle\mathcal{E}_{\text{inj}}\rangle}, \quad (16)$$

where the terms on the right are the internal efficiency, net flow efficiency, turbulent kinetic efficiency, and electromagnetic efficiency, respectively. We use $\Delta\mathcal{E}$ to indicate the change in a type of energy density since the start of the simulation, i.e. $\Delta\mathcal{E}(t) = \mathcal{E}(t) - \mathcal{E}(0)$.

Since the change in internal energy grows approximately linearly in time (as will be discussed in Section 3.2.3), we characterize the evolution by the heating rate of the plasma, i.e. the time derivative of the internal energy $\langle\dot{\mathcal{E}}_{\text{int}}\rangle(t)$. We define the dimensionless, order-unity coefficient η_{inj} , the so-called ‘‘injection efficiency’’, as the ratio of the plasma heating rate to a ‘‘reference’’ heating rate $\langle\dot{\mathcal{E}}_{\text{ref}}\rangle$. We define $\langle\dot{\mathcal{E}}_{\text{ref}}\rangle$ by dividing the turbulent magnetic energy density, $\delta B_{\text{rms}}^2/8\pi$, by a characteristic nonlinear cascade time at the outer scale $L/\delta v_{\text{rms}} \sim L/(v_{A0}\delta B_{\text{rms}}/B_0)$, assuming strong Alfvénic turbulence and $v_{A0}/c \ll 1$. This formulation gives us an operational definition of the injection efficiency in terms of quantities that can be directly measured in our simulations at any moment of time:

$$\eta_{\text{inj}} \equiv \frac{\langle\dot{\mathcal{E}}_{\text{int}}\rangle}{\langle\dot{\mathcal{E}}_{\text{ref}}\rangle} = \frac{8\pi B_0 L \langle\dot{\mathcal{E}}_{\text{int}}\rangle}{\delta B_{\text{rms}}^3 v_{A0}}. \quad (17)$$

The injection efficiency quantifies how efficiently turbulent magnetic energy cascades to small scales and dissipates.

3 RESULTS

In this section, we investigate how imbalanced turbulence differs from balanced turbulence through a series of comparisons. After demonstrating the presence of a turbulent cascade for all values of balance parameter (Section 3.1), we examine how the injected energy transforms into the plasma’s internal, turbulent, and net flow energy (Section 3.2). By using the statistical study of eight random seeds at smaller simulation domains $L/2\pi\rho_e0 = 40.7$ to enhance the trends in the largest simulation domains $L/2\pi\rho_e0 = 81.5$, we constrain the dependence of each of these energy types on balance parameter. We then explore the decomposition of the plasma energy into thermal and nonthermal components and how particle acceleration depends on the balance parameter (Section 3.3). Finally, we vary $L/2\pi\rho_e0$ to determine the influence of kinetic effects on the fluid quantities (Section 3.4).

3.1 Formation of a turbulent cascade

The spectrum of the turbulent magnetic energy is a common diagnostic when examining turbulence. Much of the previous work on imbalanced turbulence in MHD plasmas has examined the power-law indices of the two Elsasser fields and how they may or may not deviate from Goldreich-Sridhar $k_{\perp}^{-5/3}$ scalings (Goldreich & Sridhar 1995; Lithwick et al. 2007; Beresnyak & Lazarian 2008). In this study, we simply calculate the overall turbulent magnetic energy spectrum via:

$$P_{\text{mag}}(k_{\perp}, t) = \int dk_z d\phi k_{\perp} \frac{1}{8\pi} \left(|\tilde{B}_x|^2 + |\tilde{B}_y|^2 + |\delta\tilde{B}_z|^2 \right), \quad (18)$$

where $\delta B_z = B_z - B_0$, k_z are the parallel wavenumbers, ϕ are the azimuthal angles, and $\tilde{\cdot}$ indicates the Fourier transform.

We find that the magnetic energy spectrum shows the formation of a turbulent cascade for all balance parameters (Fig. 1a). The spectra averaged over the time interval $8.8 < tc/L < 9.9$ (corresponding to $5.1 < tv_{A0}/L < 5.7$), i.e. after the turbulent cascade has fully developed but before the plasma’s heating has diminished the inertial range, show similar shapes for all values of the balance parameter. The inertial range forms between $k_{\perp}\rho_e(t) \sim 0.08$ and 0.6 for the extremely imbalanced case; a slightly shifted inertial range beginning at $k_{\perp}\rho_e(t) \sim 0.15$ rather than $k_{\perp}\rho_e(t) \sim 0.08$ for the simulations with more balanced turbulence ($\xi = 1.0$ and 0.75) results from the faster heating at these balance parameters. The power-law index in the inertial range is roughly consistent with $-5/3$, the classic MHD prediction for strong turbulence (Goldreich & Sridhar 1995), but better matches the expected scaling $\propto k_{\perp}^{-2}$ for weak turbulence in the non-relativistic (Galtier et al. 2000) and relativistic (TenBarge et al. 2021; Ripperda et al. 2021) regimes. The discrepancy with previous simulations (e.g. Zhdankin et al. 2018a), which find a slope of $-5/3$, is likely due to a small domain size. Identical balanced simulations with twice the domain size are consistent with a power-law index of $-5/3$ (dark grey line in Fig. 1a). Accurately measuring the power-law indices of imbalanced turbulence via larger domain sizes is beyond the scope of the present study. Below the characteristic Larmor radius ($k_{\perp}\rho_e \gtrsim 1$), the spectrum steepens to another power law that covers a more limited range between $k_{\perp}\rho_e(t) \sim 1$ and 2 and is broadly consistent with the formation of a kinetic cascade with a power-law index of -4 for all values of imbalance (also found in Zhdankin et al. 2018a), much steeper than in the inertial range. Again, however, providing more exact values to test against the predictions and measurements in Schekochihin et al. (2009) or Zhdankin et al. (2018a) would require larger, better-resolved simulation domains. Numerical noise dominates at scales smaller than $k_{\perp}\rho_e(t) \sim 2$.

Although determining the precise dependence of the inertial range’s slope on balance parameter would require a larger inertial range, there are hints that the slope depends on ξ . When the magnetic energy spectrum is compensated by the weak turbulence scaling k_{\perp}^{-2} , the simulation with balanced turbulence ($\xi = 1.0$) has a downward-sloping spectrum, whereas the simulation of extremely-imbalanced ($\xi = 0.0$) turbulence has a slightly positive slope (Fig. 1b). The positive slope of the compensated imbalanced spectra implies that the power law becomes slightly shallower with increasing imbalance, though constraining the variation in the power-law index is difficult to quantify with such a short inertial range. Previous MHD predictions generally discuss the spectra of the Elsasser variables rather than the magnetic energy spectra, making it difficult to directly compare these predictions to our results. If the magnetic energy spectrum slope’s dependence on imbalance persists in larger simulations, it could support MHD predictions that the Elsasser variables’ power-law indices depend on imbalance (Galtier et al. 2000; Chandran 2008). MHD simulations of imbalanced turbulence have found that the spectrum of E_+ is flatter than that of E_- , but argue that the two should converge at higher Reynolds number and numerical resolution (Perez & Boldyrev 2010b; Perez et al. 2012). Measuring the spectra of Elsasser variables would allow for direct comparison to MHD predictions of imbalanced turbulence.

Further evidence for the formation of a turbulent cascade comes from comparing the evolution of the energy injected into the simulation and the internal energy of the plasma. Whereas the accumulated injected energy increases linearly from $t = 0$ onward (Fig. 2), the internal energy density does not begin to increase until about $2.5 L/c$, close to one Alfvén-crossing time (see Section 3.2.3, Fig. 3c). Pre-

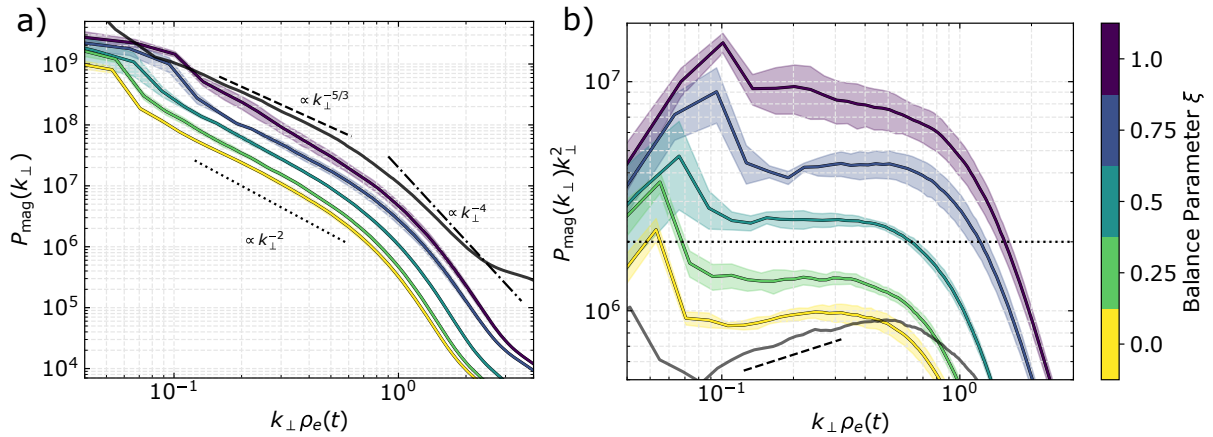


Figure 1. A turbulent cascade forms for all balance parameters. a) The magnetic energy spectra $P_{\text{mag}}(k_{\perp})$ for $L/2\pi\rho_{e0} = 81.5$ simulations of varying balance parameter averaged between times $8.8 < tc/L < 9.9$ (comprising five outputs) show an inertial range between $k_{\perp}\rho_e(t) \sim 0.1$ and 1.0 . A break in the spectrum at $k_{\perp}\rho_e(t) \sim 1.0$ indicates the onset of kinetic effects. b) When compensated by k_{\perp}^2 , the spectra for the balanced $\xi = 0.75$ and 1.0 cases are slightly steeper than $\propto k_{\perp}^{-2}$, whereas the imbalanced case $\xi = 0.0$ is slightly flatter. Shaded lines show one temporal standard deviation about the mean. Black dashed lines show the scaling $k_{\perp}^{-5/3}$; black dotted lines show k_{\perp}^{-2} . Gray lines show the $L/2\pi\rho_{e0} = 164$ balanced simulation’s magnetic energy spectrum, taken at $t = 8.9 L/c$.

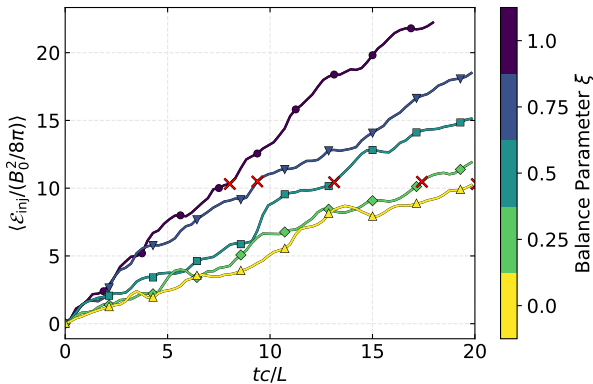


Figure 2. The amount of energy injected into a simulation depends on its balance parameter. The simulations of more balanced turbulence (purple and blue) have more injected energy than the simulations of less balanced turbulence (yellow and green). Red \times ’s indicate the “equivalent” times where the same amount of energy has been injected for each simulation (see Table 2), which all have $L/2\pi\rho_{e0} = 81.5$.

sumably the energy injected at the driving scale cascades to smaller scales over the time period $t = 0 - 2.5 L/c$ until it reaches the characteristic Larmor radius and dissipates into internal energy—i.e. the turbulent cascade forms in the first couple of light-crossing times. There appears to be an increase in the cascade formation time for decreasing balance parameter (see Section 3.2.3).

3.2 Partition of the Injected Energy

3.2.1 Framework for the Energy Partition

Because we drive the plasma in each simulation without an energy sink, the overall energy of each case increases in time. By adding a statistically-constant amount of energy at each timestep, the overall amount of injected energy increases linearly in time (Fig. 2). The amplitude of the driven waves by definition depends on the balance parameter ξ (Equation 8), and so the amount of energy injected also depends on ξ . The increase in injected energy is twice as fast for

the balanced case $\xi = 1.0$ as for the extremally-imbalanced case $\xi = 0.0$ (Fig. 2). This doubling of injected energy occurs because twice as many modes are driven in the balanced as in the extremally-imbalanced case.

The injected energy converts into various types of plasma energy, each of which will be discussed in the following subsections. Fig. 3 shows temporal evolution of each quantity’s energy density (left) and energy efficiency (right). The large-scale injected energy cascades to smaller scales in the form of bulk kinetic and electromagnetic energy until it is dissipated into internal energy, thereby implying that the internal energy should increase linearly in time during the statistical steady state—and it does, as shown in Fig. 3c. As stationary conduits for the turbulent Alfvénic cascade, we expect both the turbulent kinetic and magnetic perturbations to fluctuate around steady-state values rather than continually increasing over time. Simulations support this idea of statistically steady-state values: the turbulent electromagnetic and kinetic energies saturate to their mean values around $7.5 L/c$ and fluctuate thereafter around these values (Fig. 3a, b). These values’ dependence on balance parameter will be explored in Section 3.2.2, while the dependence of the internal energy density’s slope on balance parameter is discussed in Section 3.2.3. The final component of plasma energy, the kinetic energy of net motion through the simulation domain, does not have an easily characterized evolution (Fig. 3d); its dependence on balance parameter will be discussed in Section 3.2.4.

Normalizing the change in each type of energy to the injected energy (the energy efficiency; Equation 16) allows direct comparison between turbulence with different balance parameters while accounting for the injected energy’s dependence on ξ (Fig. 4). About 80–90% of the injected energy dissipates into internal energy over the course of our simulations, a percentage that increases over time. In contrast, the fractions of injected energy that convert into turbulent electromagnetic and kinetic energy (i.e. the electromagnetic and kinetic energy efficiencies) decrease in time as $1/t$, plotted as dashed black lines in Fig. 4, and do not seem to have drastically different magnitudes for the balanced ($\xi = 1.0$) and extremally-imbalanced ($\xi = 0.0$) case. These fits are motivated by the discussion in the previous paragraph; when normalized to the injected energy $\propto t$, these two types of turbulent energy can be fit to the function $A + B/t$. The fraction of

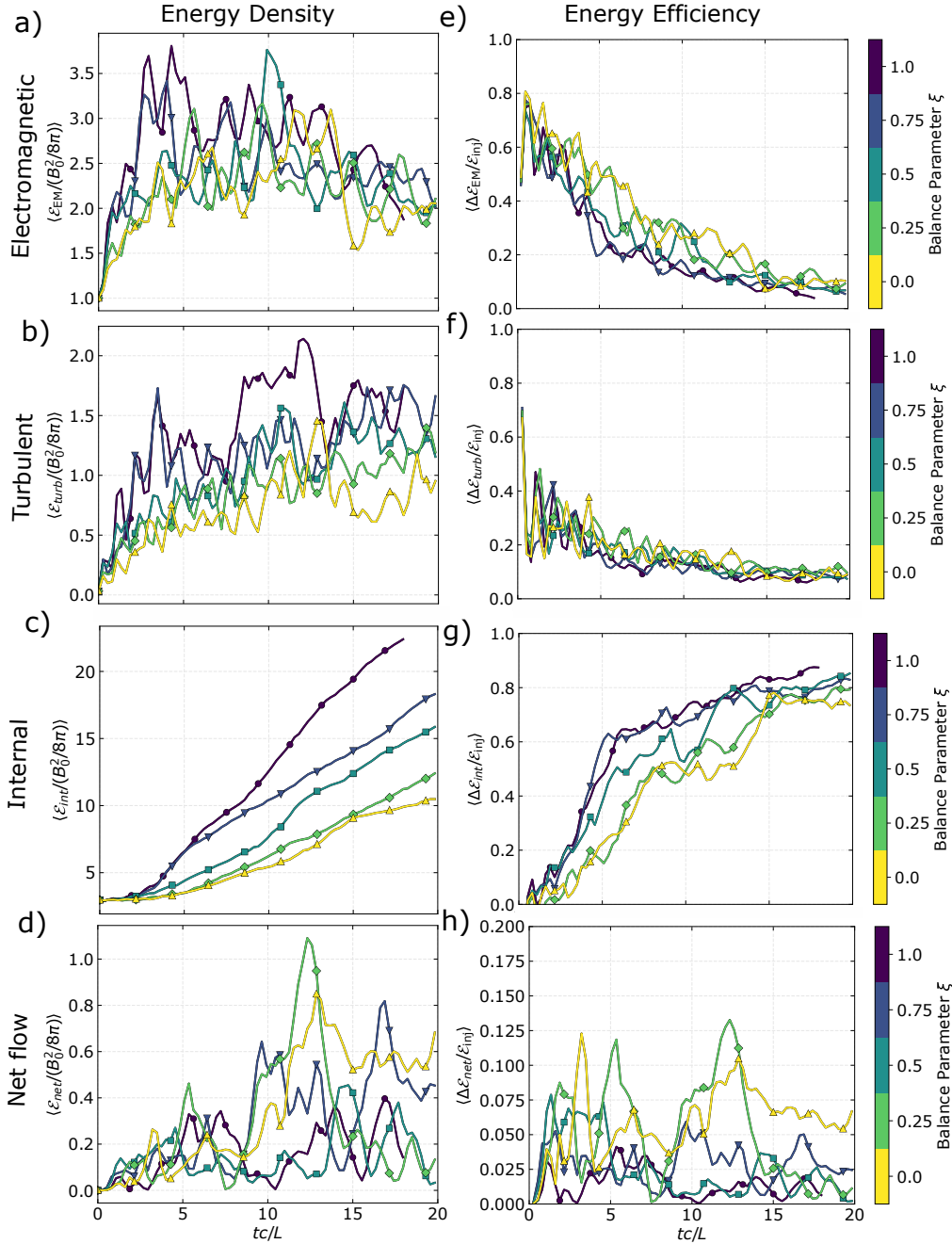


Figure 3. Energy partition into electromagnetic, turbulent kinetic, internal, and net flow energy depends on balance parameter. Left column: each type of energy density evolved over time, normalized to the constant value of the initial magnetic energy density $B_0^2/8\pi$. The turbulent electromagnetic (a) and kinetic (b) energy densities reach a constant value whereas the internal (c) and net flow (d) energy densities increase over time. Right column: the change in each type of energy density evolved over time, normalized to the total amount of injected energy density $\mathcal{E}_{\text{inj}}(t)$. Summing over the four panels on the right for each simulation adds to 1. Turbulent electromagnetic (e) and kinetic (f) energy efficiencies decay as $\propto t^{-1}$, whereas internal (g) and net flow (h) energy efficiencies saturate at a constant fraction of the injected energy. Note that the net flow energy (h) has a different vertical axis. Colors and markers indicate balance parameter. These simulations all have $L/2\pi\rho_{e0} = 81.5$.

injected energy that converts into net flow energy differs by an order of magnitude between the balanced case (1%) and the imbalanced case (10%). In both cases, however, the net flow efficiency remains relatively constant in time, indicating that a constant fraction of injected energy converts into net flow energy, with a clear dependence on ξ (also seen in Fig. 3h).

We now propose an interpretation for the constant net flow en-

ergy efficiency of imbalanced turbulence. We can estimate the net flow energy density as $\mathcal{E}_{\text{net}} \sim \langle \rho \rangle v_{\text{net}}^2/2$, where ρ is the effective relativistic mass density of the plasma and $\delta v_{\text{net}} = v_{\text{net}} \hat{z}$ is the plasma's net velocity along the background magnetic field, assumed to be not strongly relativistic. We will see in Section 3.2.4 that v_{net} is constant in time; however, the volume-averaged relativistic mass density $\langle \rho(t) \rangle = \langle \gamma \rangle(t) \rho_0 c^2$ increases linearly in time as the plasma

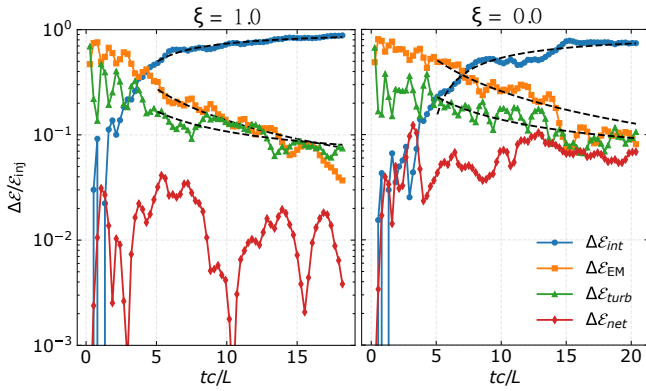


Figure 4. Time evolution of the energy partition for the balanced case ($\xi = 1.0$; left) and extremally-imbalanced case ($\xi = 0.0$; right). Both show a decay in turbulent electromagnetic and kinetic energies and a saturation of internal and net flow energy densities; black dashed lines shows fits to $A+B/t$, with A and B constants. The imbalanced case has net flow energy density about an order of magnitude higher than the balanced case and correspondingly lower internal energy density, whereas the turbulent electromagnetic and kinetic energy densities are comparable for both balance parameters.

heats (here ρ_0 is the rest mass energy density). The linear increase in \mathcal{E}_{net} leads to a constant net flow energy efficiency.

With a broad framework for the temporal evolution of internal, net, turbulent kinetic, and magnetic energy in hand, the following sections will explore each type of energy’s dependence on balance parameter using various averages and highlighting statistical variation with the random seed study.

3.2.2 Electromagnetic and Turbulent Kinetic Energy

After a transient initial period, the turbulent electromagnetic and kinetic energies become statistically constant in time (Fig. 3a, b). The electromagnetic energy increases from initially having only energy in the background magnetic field to having about the same amount of energy in the electromagnetic fluctuations as in the background field (Fig. 3a). The time-averaged magnetic energy density $\langle \Delta \mathcal{E}_{\text{mag}} \rangle$, plotted in Fig. 5a, increases as a function of balance parameter: by about 50% for turbulence in the largest simulation domain sizes. The vertical axis in Fig. 5a measures $\delta B_{\text{rms}}^2/B_0^2$, demonstrating that magnetic fluctuations are comparable to the background magnetic field for all balance parameters and that the turbulence is in the strong regime where nonlinear interactions are comparable to linear terms. In contrast, the electric energy density decreases from 10 - 25% of $B_0^2/8\pi$ for $\xi = 0.0$ to 10 - 17% for $\xi = 1.0$ (not shown). This decrease in electric energy density could be due to the decrease in the plasma velocity, which is approximately the Alfvén speed: $E \sim (\delta v/c) \times B \sim (v_A/c)B_0$. Faster heating in the balanced turbulence case leads to smaller v_A and hence smaller electric field. The simulations show that the time-averaged turbulent kinetic energy density $\langle \Delta \mathcal{E}_{\text{turb}} \rangle$ also depends on ξ , increasing from 75% of the background magnetic energy for the extremally-imbalanced case ($\xi = 0.0$) to about 125% for balanced turbulence with $\xi = 1.0$ (Fig. 5b). The smaller values of $\langle \Delta \mathcal{E}_{\text{mag}} \rangle$ and $\langle \Delta \mathcal{E}_{\text{turb}} \rangle$ in the imbalanced case result from the injection of less energy in this case (Fig. 2). The fraction of injected energy that converts into turbulent and magnetic energy (i.e. the corresponding energy efficiencies) at any given time is almost independent of balance parameter (Fig. 3e, f), with slightly higher $\langle \Delta \mathcal{E}_{\text{EM}} \rangle / \langle \mathcal{E}_{\text{inj}} \rangle$ for $\xi = 0$ compared to $\xi = 1$.

Table 1. The turbulence in all simulations of balanced and imbalanced turbulence is approximately Alfvénic. The Alfvén ratio $r_A = \langle \Delta \mathcal{E}_{\text{turb}} \rangle / \langle \Delta \mathcal{E}_{\text{mag}} \rangle$ is approximately 1 for the largest simulations ($L/2\pi\rho_{e0} = 81.5$) for all values of the balance parameter ξ . Standard deviations are calculated from the statistical seed studies at each balance parameter.

ξ	$\langle \Delta \mathcal{E}_{\text{turb}} \rangle / \langle \Delta \mathcal{E}_{\text{mag}} \rangle$
1.0	1.1 ± 0.3
0.75	1.2 ± 0.2
0.5	1.0 ± 0.1
0.25	1.0 ± 0.1
0.0	0.9 ± 0.1

To test whether the turbulence is Alfvénic, we use the “Alfvén ratio” $r_A \equiv \langle \Delta \mathcal{E}_{\text{turb}} \rangle / \langle \Delta \mathcal{E}_{\text{mag}} \rangle$. The Alfvén ratio is related to the residual energy E_r (defined as the difference between the turbulent kinetic and turbulent magnetic energies) via $E_r = (r_A - 1)/(r_A + 1)$. Ideal MHD predicts that the time- and volume-averaged kinetic and magnetic energies in an Alfvén wave should be in equipartition: $r_A = 1$. We might expect the same Alfvén ratio for turbulence (both balanced and imbalanced) comprising many Alfvén waves — though physical plasmas such as the solar wind often have an excess of magnetic energy such that $r_A \approx 0.7$ (Chen et al. 2013; Chen 2016); see Boldyrev & Perez (2009), Boldyrev et al. (2011), and Wang et al. (2011) for MHD models of this excess. Our simulations show that both balanced and imbalanced turbulence are in equipartition to within error bars (Table 1). The standard deviations of mean values for $\langle \Delta \mathcal{E}_{\text{turb}} \rangle$ and $\langle \Delta \mathcal{E}_{\text{mag}} \rangle$ in Table 1 were calculated for the $L/2\pi\rho_{e0} = 81.5$ and $L/2\pi\rho_{e0} = 40.7$ simulations (nine values for each balance parameter) and summed in quadrature. These error bars suggest that the large-scale ratio of turbulent kinetic to magnetic energies is independent of ξ . However, the residual energy may have a scale-dependent power-law spectrum with significant dependence on imbalance, which we do not address here. The solar wind shows a clear dependence of the residual energy spectrum’s slope on imbalance, with a value of -2 for balanced turbulence and closer to -1.8 for totally imbalanced turbulence (Chen et al. 2013). The dependence of the residual energy spectrum’s slope on imbalance is a major outstanding puzzle that has not been successfully addressed by any phenomenological model of imbalanced turbulence thus far.

Our finding of approximate equipartition is particularly important because the turbulence is not quite incompressible, with fluctuations in the total density on the order of 20-30% of the background density (not shown). The higher density fluctuations are expected in the relativistic regime due to the coupling of the Alfvénic and fast modes (Takamoto & Lazarian 2016). Solenoidal driving (Zhdankin 2021) could help further test whether these compressible modes affect the Alfvén ratio measured in our simulations. For now, we conclude that the turbulence in our simulations can be considered predominately Alfvénic.

3.2.3 Internal Energy

The increase in internal energy dominates the plasma energy budget at late times. Though the initial internal energy starts out at about three times the initial magnetic energy for all balance parameters, the plasmas with balanced turbulence heat up almost twice as quickly as the plasmas with imbalanced turbulence (Fig. 3c). About 80% of the injected energy is converted into internal energy in the imbalanced

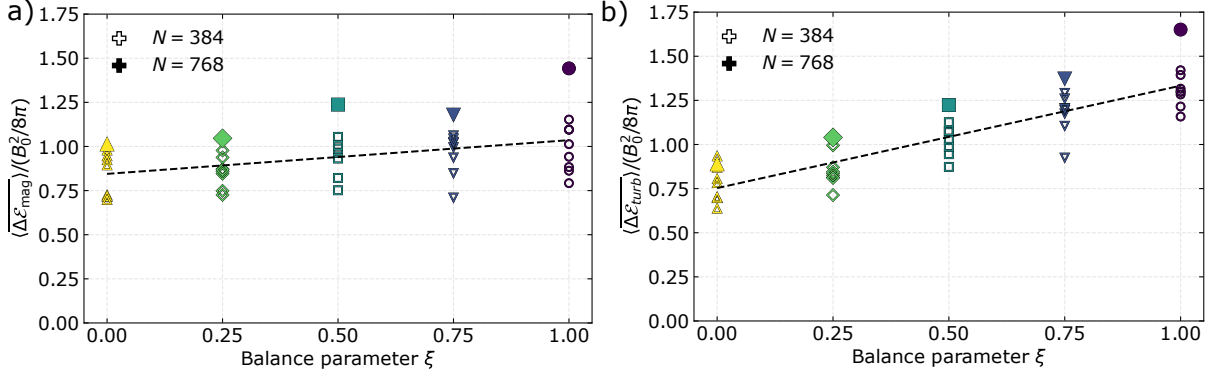


Figure 5. Trends of the turbulent magnetic and kinetic energy densities with balance parameter. Quantities are time-averaged from $10 < tc/L < 20$. The largest domain size $L/2\pi\rho_{e0} = 81.5$ (filled markers) shows a linear trend with balance parameter for the turbulent magnetic (a) and kinetic (b) energy densities, respectively. The statistical deviation is shown by the $L/2\pi\rho_{e0} = 40.7$ seed study (unfilled markers). The dashed lines show linear fits. Colors and markers are the same as in Fig. 3.

case ($\xi = 0$), slightly lower than the corresponding value of closer to 90% for the balanced case (Fig. 3g). Because the plasma’s internal energy increases linearly after an initial transient, we characterize its heating rate (i.e. slope) through the “injection efficiency” parameter η_{inj} (Equation 17). The heating rate of the plasma is extracted by fitting the slope of the internal energy in the interval $5 < tc/L < 20$ and converting to the injection efficiency via Equation 17, taking the value of δB_{rms} as the time-average over the same time period. The statistical mean value of the injection efficiency varies from about 1.0 for the extremally-imbalanced case ($\xi = 0.0$) to about 1.5 for the balanced case ($\xi = 1.0$) as seen in Fig. 6a, with a statistical standard deviation on the order of 0.2.

As discussed in Section 3.2.2, the magnitude of the magnetic field fluctuations depends on balance parameter, which in principle may influence energy dissipation and the injection efficiency. To verify that the trend in the injection efficiency η_{inj} with balance parameter ξ is not due to the variation of the amplitude of magnetic energy perturbations $\delta B_{\text{rms}}^2/B_0^2$ with ξ , we ran a simulation of imbalanced turbulence with $\xi = 0$ and a driving amplitude $\sqrt{2}$ times its canonical value. The magnetic field fluctuation level δB_{rms}^2 changes from $0.8B_0^2$ for the unadjusted amplitude case to $1.2B_0^2$ for the increased amplitude case, consistent with the unadjusted amplitude of the balanced case with the same random seed. The injection efficiency, however, increases to 1.1 with the increased amplitude, compared to 0.9 for the unadjusted $\xi = 0$ case and 1.4 for the unadjusted $\xi = 1$ case with the same random seed. Thus, two simulations with the same level of magnetic field perturbations but different balance parameters experience significantly different injection efficiencies, suggesting that the injection efficiency has an inherent dependence on balance parameter rather than δB_{rms} . This result suggests that the cascade time depends on balance parameter, which we turn to next.

To explore the possibility that the cascade time τ_{casc} depends on balance parameter, we define

$$\tau_{\text{casc}} \equiv \frac{\langle \Delta \mathcal{E}_{\text{EM}} + \mathcal{E}_{\text{turb}} \rangle}{\langle \dot{\mathcal{E}}_{\text{int}} \rangle}. \quad (19)$$

The cascade time is normalized to the global Alfvén time $L/v_A(t)$ and then time-averaged over $10 < tc/L < 20$ (i.e. $5.8 < tv_{A0}/L < 11.6$). We expect the cascade time to be on the order of an Alfvén time for an Alfvénic cascade, and for balanced turbulence we indeed find that the cascade time varies statistically between 0.8 and 1.2 $L/v_A(t)$ (Fig. 6b). However, the cascade time increases to about 2.2 $L/v_A(t)$

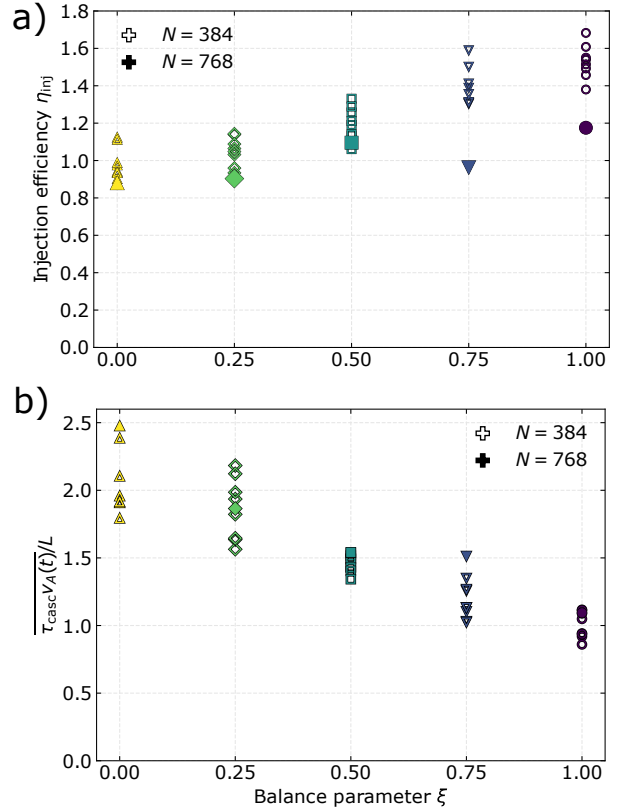


Figure 6. The injection efficiency η_{inj} (a; Equation 17) and cascade time τ_{casc} (b; Equation 19) depend on balance parameter. The largest domain size $L/2\pi\rho_{e0} = 81.5$ is shown with filled markers and the statistical deviation is shown by the $L/2\pi\rho_{e0} = 40.7$ seed study (unfilled markers). Colors and markers are the same as in Fig. 3.

on average for the imbalanced case $\xi = 0$. The lack of overlap between the cascade times of imbalanced and balanced turbulence suggest that the difference is statistically significant, rather than a fluke of random seeds. A longer cascade time for more imbalanced turbulence is consistent with, for instance, Lithwick et al. (2007)’s suggestion that the dominant waves are less strongly scattered in the imbalanced case.

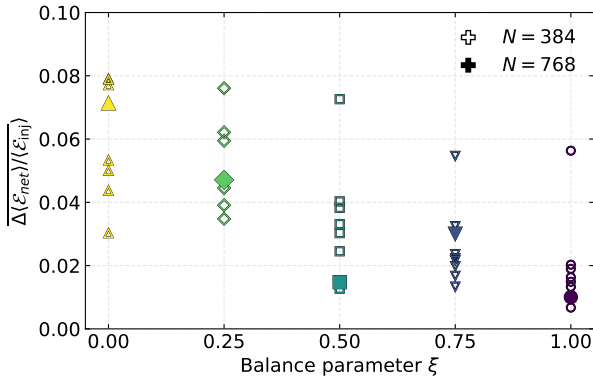


Figure 7. The net flow energy efficiency decreases with increasing balance parameter. The plotted values are volume-averaged and time-averaged from $10 < tc/L < 20$. The largest domain size $L/2\pi\rho_{e0} = 81.5$ is shown with filled markers and the statistical deviation is shown by the $L/2\pi\rho_{e0} = 40.7$ seed study (unfilled markers). Note that the outliers for $\xi = 0.5, 0.75$, and 1.0 with net flow energy efficiencies a factor of 2 higher than the rest of the seed study were run with the same random seed. Colors and markers are the same as in Fig. 3.

3.2.4 Net Flow Energy

As a component of the energy not present in balanced turbulence, we expect the kinetic energy in the net motion of the plasma through the simulation domain to depend on the balance parameter. In the balanced case, the statistically-symmetric (although not necessarily momentum-conserving) driving should on average lead to no net motion. In contrast, because imbalanced driving breaks the symmetry along the background magnetic field, we may expect a nonzero net flow energy for $\xi < 1.0$ if the asymmetric injected momentum converts into plasma momentum. Our simulations find that about 8% of the injected energy converts into net flow energy even in the extremally-imbalanced case ($\xi = 0.0$), a fraction that becomes comparable to the turbulent electromagnetic or kinetic energy efficiencies after the latter two have decayed by a factor of two or more, around $15 L/c$ (Fig. 4). Since the net flow efficiency fluctuates strongly about a mean value in time, we compare different balance parameters by averaging over $10 < tc/L < 20$. The result, shown in Fig. 7, reveals that the net flow efficiency increases with decreasing ξ , as expected. The mean over an ensemble of identical extremally-imbalanced simulations with varying random seeds is about 0.06, approximately three times as large as that for the balanced turbulence (about 0.02). The statistical spread in the balanced case is on the order of 0.01, and about 0.03 for the imbalanced case. Because energy is a strictly positive quantity and a limited number of modes were driven, even the simulations of balanced turbulence ($\xi = 1.0$) have a non-zero (albeit small) net flow energy due to short periods of net motion. Notably, there are three prominent outliers in Fig. 7 in the magnitude of the net flow efficiency in simulations with balance parameters $\xi = 0.5, 0.75$, and 1.0 . Each of these outlying simulations was initialized with the same random seed, suggesting that the particular random phases of the driven modes resulted in non-zero mean velocity later in the simulations' evolutions. The presence of these outliers demonstrates the need for a suite of random seeds to tease out statistically-robust trends.

Although the net flow energy density demonstrates the importance of the net flow in the overall energy budget, it does not contain information about the direction of the plasma's net motion. To address this issue, we now examine momentum rather than energy. First,

we discuss the electromagnetic momentum and look at the Poynting flux $\mathbf{S} = (c/4\pi)\mathbf{E} \times \mathbf{B}$. For balance parameters $\xi < 1.0$, we expect the driven waves' Poynting flux to be nonzero along the background magnetic field ("parallel Poynting flux"; S_z). The spatial distribution of the parallel Poynting flux, plotted in Fig. 8, is highly nonuniform. Similar to MHD turbulence (Perez & Boldyrev 2009), our balanced simulation has local patches of strong Poynting flux and thus high imbalance, highlighting the fundamental connection between balanced and imbalanced turbulence at small scales. The total, volume-averaged parallel Poynting flux $\langle S_z \rangle$ is statistically constant in time and, for the balanced case ($\xi = 1.0$), oscillates around zero (Fig. 9a). After time-averaging over the period from $10 < tc/L < 20$, the parallel Poynting flux is clearly positive for imbalanced turbulence and consistent with zero for balanced turbulence (Fig. 9b). The value $\langle S_z \rangle \approx 0.2 (cB_0^2/4\pi)$ at $\xi = 0.0$ is about 30% of the limiting value $(\delta B/B_0)^2 v_A/c (cB_0^2/4\pi) \approx v_A/c (cB_0^2/4\pi) \approx 0.58 (cB_0^2/4\pi)$ expected for a single Alfvén wave (Equation 10). The decrease in the Poynting flux with increasing balance parameter agrees well with the quadratic fit predicted by Equation 11, as shown by the dotted and dash-dot black lines in Fig. 9b, though we do not rule out a linear dependence. The same outliers discussed for the net flow efficiency are present in the parallel Poynting flux. The time- and volume-averaged Poynting flux in the x - and y -directions are much smaller than the parallel Poynting flux: within $0.1 (cB_0^2/4\pi)$ of zero for all balance parameters (not shown), indicating that the net electromagnetic momentum is primarily along the background magnetic field.

The injected Poynting flux imparts net momentum to the plasma. In agreement with the interpretation in Section 3.2.1, the volume-averaged parallel momentum $\langle \mathcal{P}_{z,\text{tot}} \rangle$ of the plasma increases approximately linearly over time (Fig. 9c). The ratio $\langle \mathcal{P}_{z,\text{tot}} c^2 \rangle / (\langle S_z \rangle t v_{A0} / L)$, shown in Fig. 9d, is approximately constant in time and fluctuates around values of order unity for any given balance parameter. In this figure, the parallel Poynting flux has been converted to an electromagnetic momentum density $\langle S_z \rangle / c^2$, and the momentum densities of both the plasma and the electromagnetic waves are normalized to $g_0 \equiv B_0^2 / (4\pi c)$, allowing for direct comparison between the two quantities. The ratio of the volume averages has been smoothed with a Hanning window to remove arbitrarily large values due to a small Poynting flux. To further illustrate the relationship between $\langle S_z \rangle$ and $\langle \mathcal{P}_{z,\text{tot}} \rangle$, Fig. 10 shows their values at each time snapshot (given by individual dots) for each balance parameter (shown via marker and color). In general, the plasma momentum dominates over the electromagnetic momentum, with a time-dependent ratio given by the slope of the linear fit. The positive ratio shows that a positive volume-averaged parallel electromagnetic momentum corresponds to a positive parallel plasma momentum, as expected if Poynting flux converts to plasma momentum. The balanced turbulence's electromagnetic momentum and plasma momentum span both positive and negative values; for more imbalanced turbulence, the distribution shifts up and right, demonstrating that the asymmetric driving of electromagnetic momentum results in asymmetric net motion of the plasma in the z -direction.

The magnitude of the net flow's velocity can be obtained by considering the framework outlined in Section 3.2.1. Assuming that the net velocity $v_{\text{net}}(t) \ll c$, we can write the net flow energy density as

$$\mathcal{E}_{\text{net}}(t) \approx \langle \rho \rangle (t) \frac{v_{\text{net}}^2(t)}{2} \sim \frac{\langle \mathcal{E}_{\text{int}} \rangle (t) v_{\text{net}}^2(t)}{2c^2}. \quad (20)$$

From the known values of $\mathcal{E}_{\text{net}}(t)$ and $\langle \mathcal{E}_{\text{int}} \rangle (t)$, we can estimate the magnitude of the net velocity $v_{\text{net}}(t)$. Analogously, the internal

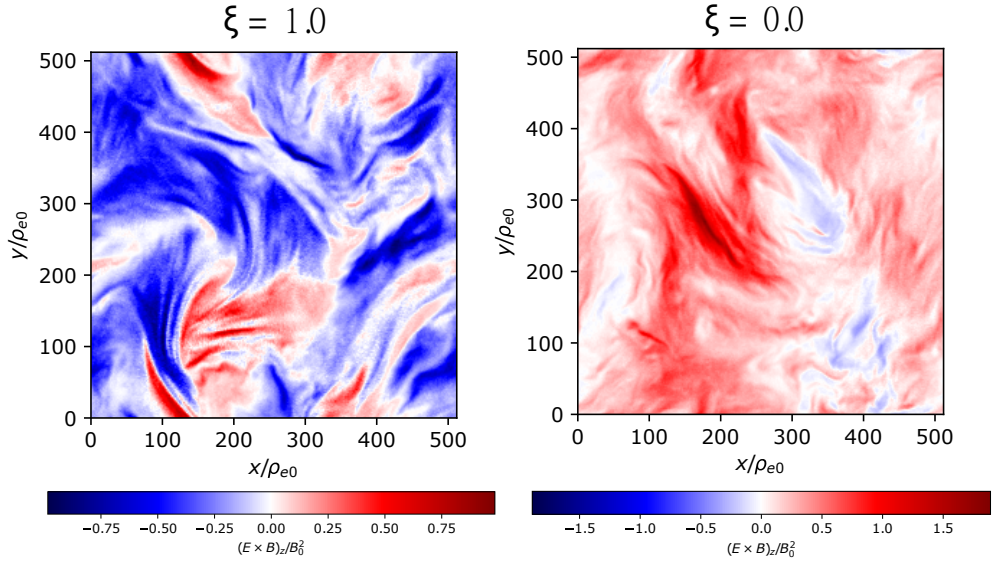


Figure 8. Even turbulence that is balanced as a whole has spatial and temporal pockets of locally imbalanced turbulence. Slices of the Poynting flux $(c/4\pi)\mathbf{E}\times\mathbf{B}$ in the z -direction, taken at the plane $z = 0$ at time $t = 16.1 L/c$ and normalized to $(c/4\pi)B_0^2$ for balanced turbulence ($\xi = 1.0$; left) and the extremely-imbalanced turbulence ($\xi = 0.0$; right) show variation in the sign of Poynting flux throughout the domain.

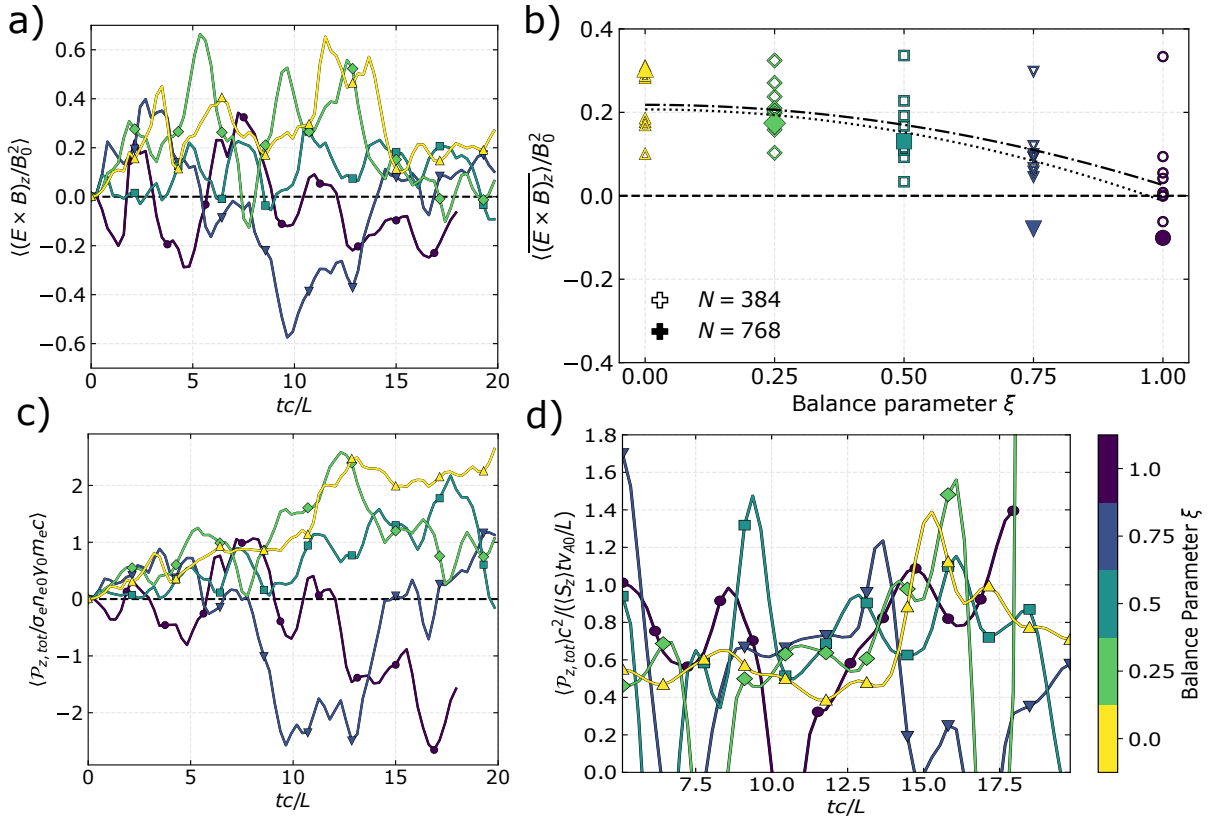


Figure 9. The average parallel Poynting flux is approximately constant in time, whereas the z -momentum of the plasma increases linearly in time. a) The time evolution of the volume-averaged Poynting flux $(c/4\pi)\langle\mathbf{E}\times\mathbf{B}\rangle$ in the z -direction, normalized to $(c/4\pi)B_0^2$, shows fluctuations around some mean value; time-averaging the curves over $10 < tc/L < 20$ shows a quadratic dependence on balance parameter (b). The time evolution (c) of the parallel plasma momentum shows an increase in time. The ratio $\langle P_{z, \text{tot}} \rangle c^2 / (\langle S_z \rangle tv_{A0}/L)$, shown in (d), is of order unity for all values of balance parameter. Black dash-dot lines show a quadratic fit; the dotted line is a quadratic fit without the outlier seed. Dashed black lines indicate zero. Colors and markers are the same as in Fig. 3.

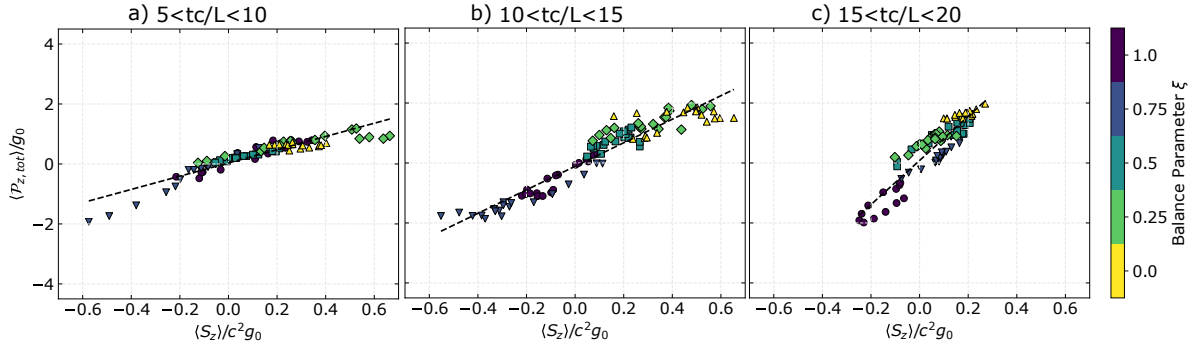


Figure 10. The parallel electromagnetic momentum generates and maintains the parallel momentum of the plasma. In these plots, each point corresponds to the instantaneous values of the volume-averaged plasma momentum along the background magnetic field and the volume-averaged parallel electromagnetic momentum at a given simulation time. Three periods of time are shown with linear fits of slopes 2.2, 3.9, and 7.4 for (a) $5 < tc/L < 10$, (b) $10 < tc/L < 15$, and (c) $15 < tc/L < 20$, respectively. Here, $g_0 = B_0^2/(4\pi c)$ is a typical value of momentum density. Colors and markers are the same as in Fig. 3.

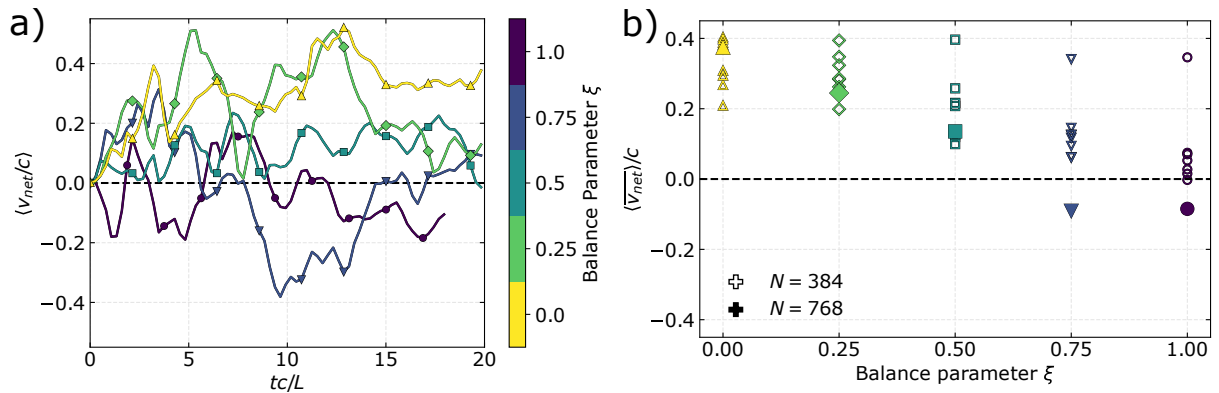


Figure 11. The net plasma velocity along the background magnetic field depends on balance parameter. a) The time evolution of the volume-averaged velocity v_{net} (Equation 21) shows values that fluctuate in time around some mean value that depends on ξ ; time-averaging the curves over $10 < tc/L < 20$ shows a dependence on balance parameter (b). The largest domain size $L/2\pi\rho_{e0} = 81.5$ is shown with filled markers and the statistical deviation is shown by the $L/2\pi\rho_{e0} = 40.7$ seed study (unfilled markers). Colors and markers are the same as in Fig. 3. Black dashed lines show zero.

energy density relates to the net plasma momentum density as

$$\langle \mathcal{P}_{z,\text{tot}} \rangle(t) \approx \langle \rho \rangle(t) v_{\text{net}}(t) \approx \frac{\langle \mathcal{E}_{\text{int}} \rangle(t)}{c^2} v_{\text{net}}(t). \quad (21)$$

The increase in the net flow energy density over time could be due to either an increase in $\langle \rho \rangle \approx \langle \mathcal{E}_{\text{int}} \rangle/c^2$, or an increase in v_{net} , or both. Using Equation 21 to solve for the velocity along the background magnetic field in our simulations, we see that after the turbulence has developed, v_{net} does not increase linearly but rather oscillates around a mean value dependent on balance parameter (Fig. 11a). This finding suggests that the increase in net flow energy density is predominantly driven by the increase in internal energy density at constant velocity. The constancy of v_{net} makes sense because both the relativistic momentum and kinetic energy increase linearly over time but depend on different powers of v_{net} . The net velocity of the plasma with balanced turbulence oscillates around zero, never reaching more than $0.2c$. The plasmas with the most imbalanced turbulence can reach net velocities up to $0.5c$. Averaging over $10 < tc/L < 20$ shows a clear dependence of the net velocity on balance parameter (Fig. 11b). As expected, plasmas with balanced turbulence experience a time-averaged net velocity near zero, though they temporarily move parallel or anti-parallel to the background magnetic field. In contrast, the most imbalanced turbulence results in plasma motion

along the background magnetic field of almost $0.4c$ on average. Such rapid net motion of the plasma may have implications for driving accretion disk winds, particularly if the wind comprises mostly non-thermal particles. Previous studies of imbalanced turbulence appear to exclude the possibility of generating net plasma motion along the background magnetic field, either through the assumption of reduced MHD, gyrokinetics, or force-free description (Cho & Lazarian 2014; Perez et al. 2012; Meyrand et al. 2020). As such, this work presents, to our knowledge, the first numerical demonstration and investigation of net flow due to imbalanced turbulence. We expect the net motion of the plasma to decrease at smaller σ : combining Eqns. 10 and 21 leads to $v_{\text{net}}/v_A \sim \sigma$. In the sense that the net flow disappears when $\sigma = 0$, the net motion of the plasma is a relativistic effect.

3.3 Nonthermal Particle Acceleration

We find that imbalanced turbulence can accelerate a significant portion of the plasma's particles to suprathermal energies (Fig. 12), much like balanced turbulence at similar magnetizations $\sigma \sim 1$. Even the extremally-imbalanced case $\xi = 0.0$ shows the development of a high-energy power-law tail, which hardens and reaches an asymptotic slope after about $12 L/c$ (Fig. 12a). The heating of the plasma is also evident in Fig. 12a, since the peak Lorentz factor

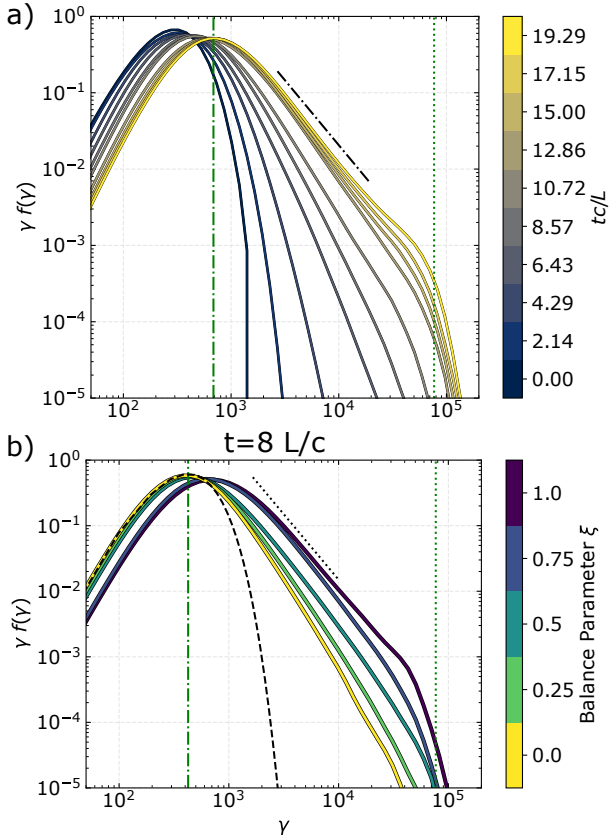


Figure 12. Particle acceleration occurs for all values of balance parameter. a) The distribution function of the extremally-imbalanced case ($\xi = 0.0$) becomes shallower in time from an initial Maxwell-Jüttner distribution (purple) to a Maxwell-Jüttner distribution plus a hard power-law component at later times (yellow). b) Spectra taken at the same time $t = 8.0 L/c$ for different balance parameters show different peak energies but similar power-law components. The dashed black line shows a Maxwell-Jüttner fit to the $\xi = 0.0$ case. The vertical green dash-dot line shows the mean Lorentz factor $\langle \gamma \rangle$ extracted from this fit. The vertical green dotted line shows the maximum energy γ_{\max} . The dash-dot black line in panel (a) shows the power law $\gamma^{-2.7}$, while the dotted black line in panel (b) shows γ^{-3} . Colors are the same as in Fig. 3.

moves from an initial value of 300 to more than 700 at the final time $t = 20 L/c$. At late times $t \gtrsim 12 L/c$, the simulation domain's boundary conditions limit the maximum attainable Lorentz factor to $\gamma_{\max} = LeB_0/m_e c^2$, resulting in the “pile-up” of high-energy particles at γ_{\max} , followed by a sharp cutoff rather than the continuation of the power law to even higher energies (Zhdankin et al. 2018b). Visually, the nonthermal distribution matches the power-law scaling $f(\gamma) \propto \gamma^{-2.7}$ between $\langle \gamma \rangle$ and γ_{\max} , shown by the dash-dot line in Fig. 12a. Comparing turbulence with different balance parameters, we see that more balanced turbulence heats the plasma more quickly and forms a power-law spectrum faster than imbalanced turbulence (Fig. 12b). For particle spectra taken at $t = 8.0 L/c$, the simulation of balanced turbulence $\xi = 1.0$ has already heated to a peak Lorentz factor of about 700 and is experiencing pile-up, as shown by the spectrum's break around $\gamma \sim 5 \times 10^4$. In contrast, the extremally-imbalanced case $\xi = 0.0$ still has a peak Lorentz factor of around 400 and its power-law index has not yet reached an asymptotic value (Fig. 12b).

Because of the different rates at which energy is injected into

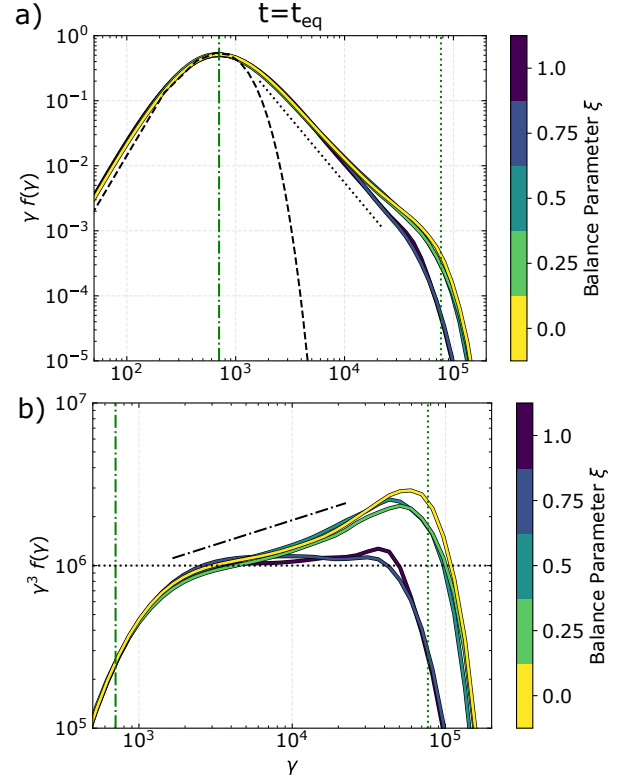


Figure 13. At equivalent times, the power laws of imbalanced turbulence are slightly flatter/harder than balanced turbulence. a) The particle energy spectra at equivalent times (see Table 2) show a similar mean energy and similar power laws until $\gamma \sim 10^4$. The dashed black line shows a Maxwell-Jüttner fit to the $\xi = 0.0$ case. b) Compensating by γ^3 reveals that more imbalanced turbulence ($\xi = 0.0, 0.25$, and 0.5) has flatter power laws than the more balanced turbulence with $\xi = 0.75$ or 1.0 . The vertical green dash-dot line shows the mean Lorentz factor $\langle \gamma \rangle$ extracted from the Maxwell-Jüttner fit. The vertical green dotted line shows the maximum energy γ_{\max} . The black dash-dot line in panel (b) shows the spectrum compensated to γ^{-3} , while the dotted black line shows the power law γ^{-3+3} (a constant). Colors are the same as in Fig. 3.

Table 2. Table of “equivalent” times t_{eq} in L/c where the same amount of energy density $10.3 B_0^2/8\pi$ has been injected. Values of the nonthermal particle and energy fraction at t_{eq} , shown in the second and third rows, are discussed in Section 3.3. Equivalent times are labelled in Fig. 2 as red \times 's.

ξ	0.0	0.25	0.5	0.75	1.0
t_{eq}	20.0	17.4	13.1	9.4	8.0
$N_{\text{nonthermal}}/N_{\text{total}}$	0.20	0.19	0.20	0.21	0.21
$\langle \mathcal{E}_{\text{nonthermal}} \rangle / \langle \mathcal{E}_{\text{pl}} \rangle$	0.54	0.53	0.55	0.54	0.54

simulations with different balance parameters, it may be more meaningful to compare particle spectra not at the same fixed absolute time, but rather at “equivalent times” when a fixed amount of energy has been injected. For definiteness, we take this time to coincide with the end ($t = 20 L/c$) of the simulation for the extremally imbalanced case, $\xi = 0$, corresponding to an injected energy of $10.3 B_0^2/8\pi$. The equivalent times for the simulations vary from $8 L/c$ for the balanced case $\xi = 1.0$ to $20 L/c$ for the extremally-imbalanced case $\xi = 0.0$ (Table 2). When compared at these equivalent times, particle spectra for different ξ essentially collapse to a single universal curve (Fig. 13a). In particular, the peak Lorentz factors and the power-law tails up to $\gamma \approx 10^4$ become nearly indistinguishable. This similarity

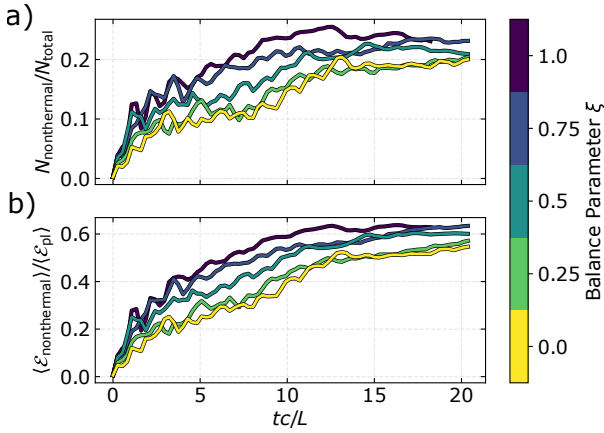


Figure 14. The partition of plasma energy $\langle \mathcal{E}_{\text{pl}} \rangle$ into thermal and nonthermal components shows a moderate increase with the balance parameter at any given time. Both the fraction of particles with nonthermal energies (a) and the fraction of total plasma energy density $\langle \mathcal{E}_{\text{pl}} \rangle$ contained in such particles (b) are calculated by fitting a thermal Maxwell-Jüttner function to the low- and medium-energy particle distribution at each time and subtracting the fit from the total particle distribution. Colors are the same as in Fig. 3.

suggests that NTPA operates similarly in balanced and imbalanced turbulence. In particular, the nonthermal segments of the distribution function match the power-law scaling $f(\gamma) \propto \gamma^{-3}$ (dotted line) for all values of balance parameter, suggesting that imbalanced and balanced turbulence accelerate particles with the same asymptotic spectra. Finer differences appear at higher energies when the spectra are compensated by γ^3 ; whereas the balanced cases $\xi = 1.0$ and 0.75 closely follow this γ^{-3} scaling in the interval $200 \lesssim \gamma \lesssim 4 \times 10^4$, the more imbalanced cases are never quite flat and appear to more closely follow the scaling $\gamma^{-2.7}$ (dash-dot line), as shown in Fig. 13b. This power-law index of -2.7 matches the power-law index of balanced turbulence particle spectra in smaller box sizes (Zhdankin et al. 2018b), suggesting that pile-up contaminates the spectra. Because the equivalent times for the simulations of imbalanced turbulence are much longer, the high-energy pile-up could be due to a small sub-population of particles whose stochastic scattering events pushed them to higher energies. Larger simulation domains are needed to determine what influence the high-energy particle pile-up could have on the particle spectra at lower energies.

The partition of the plasma particles' energy $\langle \mathcal{E}_{\text{pl}} \rangle(t)$ into thermal and nonthermal components further demonstrates that nonthermal particles are energetically important in the system. The fraction of nonthermal particles is calculated by subtracting the Maxwell-Jüttner distribution that best fits the total, box-averaged particle distribution up to the peak Lorentz factor from the total distribution function. This fraction reaches 20% of the total number of particles at $20 L/c$ for the $\xi = 0$ case (Fig. 14a). The balanced case's fraction of nonthermal particles is larger, reaching 25% of the total number of particles by the same time. At $20 L/c$, the energy in these particles comprises 55% of the total plasma energy in the imbalanced case, as compared to 65% for the balanced case (Fig. 14b). At equivalent times, the nonthermal fractions of particles and energy do not vary more than 2% across balance parameters (Table 2), suggesting that particle acceleration by imbalanced turbulence is just as efficient as acceleration by balanced turbulence. For comparison, the fractions for the balanced simulations are slightly smaller than those found for similar simulations of electron-ion plasmas in the relativistically-hot limit (Zhdankin et al. 2019).

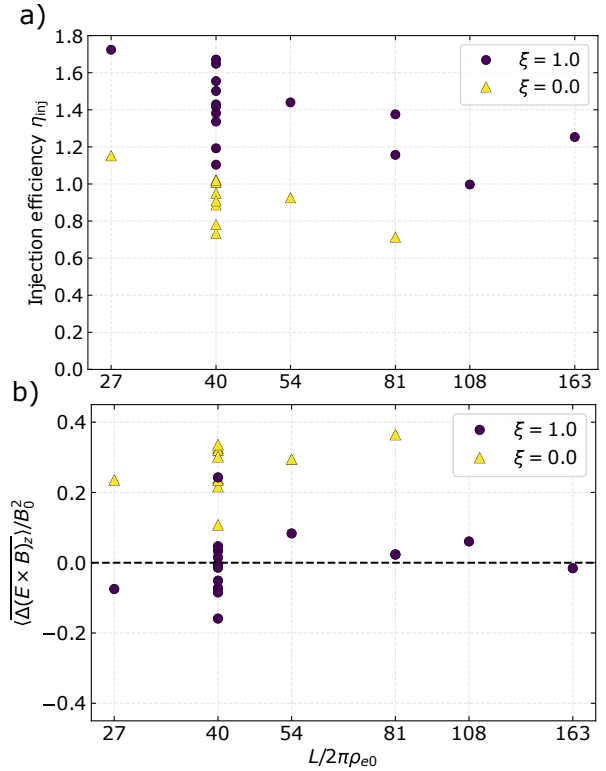


Figure 15. The injection efficiency and Poynting flux along the background magnetic field depend weakly on simulation domain size within statistical variation. When averaged from $t = 5 - 14 L/c$, the injection efficiency (a) and Poynting flux along the background magnetic field (b) are shown as a function of $L/2\pi\rho_{e0}$. Both the balanced ($\xi = 1.0$; purple circles) and extremally-imbalanced values ($\xi = 0$; yellow triangles) are mostly within statistical variation of the $L/2\pi\rho_{e0} = 40.7$ sample of 8 random seeds. The black dashed line indicates zero.

3.4 Dependence on Simulation Domain Size

If the ratio $L/2\pi\rho_{e0}$ is small, the small separation between the characteristic scale of kinetic effects and the system size scale could influence the results presented in previous sections. In this subsection, we examine the box-size dependence of representative quantities for extremal values of the balance parameter $\xi = 0.0$ and $\xi = 1.0$ and for $L/2\pi\rho_{e0} \in \{27.1, 40.7, 54.3, 81.5\}$, corresponding to $N \in \{256, 384, 512, 768\}$. These results also include three very large simulations of balanced turbulence from Zhdankin et al. (2018b) with $L/2\pi\rho_{e0} \in \{81.5, 108.7, 164\}$ ($N = 768, 1024, \text{ and } 1536$, respectively) that are otherwise identical to the other simulations of balanced turbulence in the present work. The time-averaging window has been changed from $10 < tc/L < 20$ to $5 < tc/L < 14$, because $14 L/c$ is the latest time included in all simulations. Here we focus on the convergence of energetic quantities. The convergence of the particle energy spectra with system size for balanced turbulence was discussed in Zhdankin et al. (2018b).

We find that the injection efficiency η_{inj} depends weakly on simulation domain size for both balanced and extremally-imbalanced turbulence (Fig. 15a). The simulations of balanced turbulence with $L/2\pi\rho_{e0} = 81.5$ and 164 domains have slightly lower injection efficiencies than those for the smallest ($L/2\pi\rho_{e0} = 40.7$) domains. Kinetic damping of large-scale fluctuations, which would drain energy faster than turbulence alone, may explain the larger η_{inj} for smaller domain sizes. For the imbalanced case, the $L/2\pi\rho_{e0} = 54.3$

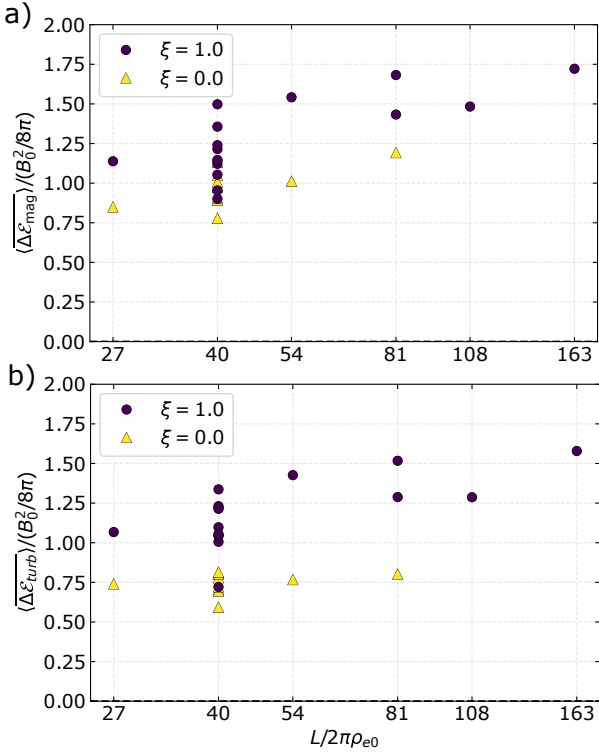


Figure 16. The magnetic and turbulent kinetic densities are weakly dependent on simulation domain size. When averaged from $t = 5 - 14 L/c$, the magnetic energy density (a) and turbulent kinetic energy density (b) are shown as a function of $L/2\pi\rho_{e0}$. Both the balanced ($\xi = 1.0$; purple circles) and extremely-imbalanced ($\xi = 0$; yellow triangles) values are mostly within statistical variation of the $L/2\pi\rho_{e0} = 40.7$ sample of 8 random seeds.

simulation’s η_{inj} is within the statistical spread of the $L/2\pi\rho_{e0} = 40.7$ simulations’ injection efficiencies, whereas the $L/2\pi\rho_{e0} = 81.5$ injection efficiency is slightly below. The time-averaged Poynting flux shows a weak positive trend with increasing domain size (Fig. 15b). Though the $L/2\pi\rho_{e0} = 81.5$ domain size for the imbalanced $\xi = 0$ case has a value higher than the largest $L/2\pi\rho_{e0} = 40.7$ value, the difference is only about 0.05 ($cB_0^2/4\pi$) (about 15%), within two standard deviations of the statistical variation shown by the $L/2\pi\rho_{e0} = 40.7$ study.

The turbulent and magnetic energy densities show a slight dependence on simulation domain size (Fig. 16). Both quantities’ values for $L/2\pi\rho_{e0} \geq 54.3$ are consistently about 15% greater than the largest value of the statistical ensemble of $L/2\pi\rho_{e0} = 40.7$, $\xi = 1.0$ simulations. Though the imbalanced turbulence simulations do not appear to exhibit a trend in turbulent kinetic energy with box size (Fig. 16b), the $L/2\pi\rho_{e0} = 81.5$, $\xi = 0$ case’s value for magnetic energy is noticeably (20%) higher than the $L/2\pi\rho_{e0} = 54.3$ value, which lies within the statistical spread of the $L/2\pi\rho_{e0} = 40.7$ ensemble study (Fig. 16a).

4 CONCLUSIONS

In this study we investigate, for the first time, imbalanced kinetic turbulence in a collisionless, magnetized, relativistically hot plasma. We employ PIC simulations to drive large-scale external current waves in a pair plasma, creating Alfvén waves propagating parallel and anti-parallel to the background magnetic field with different amplitudes.

We demonstrate the formation of a turbulent cascade for all values of the balance parameter covered by the simulations and show a slight hardening of the power law with higher imbalance (Section 3.1). We find that the energy injected into the plasma by the external driving is not only converted into internal energy through small-scale dissipative processes (Section 3.2.3), but also drives net bulk motion of the plasma (Section 3.2.4). We also find efficient particle acceleration over two decades of particle Lorentz factor even for turbulence with totally-imbalanced driving (Section 3.3), whereas quasi-linear analytical models of turbulent particle acceleration suggest that turbulent NTPA cannot operate in totally imbalanced turbulence (Schlickeiser 1989; Chandran 2000).

Our results on imbalanced turbulence should apply to high-energy astrophysical systems with asymmetric energy injection, such as accretion disk coronae, relativistic jets, and pulsar wind nebulae. Our finding that the momentum from the driven Alfvén waves efficiently transfers to the plasma itself has applications to launching a wind from the surface of a turbulent accretion disk. Depending on the relative importance of magnetocentrifugal winds (Blandford & Payne 1982) and other wind-driving mechanisms, our results on launching an Alfvén wave-driven net flow could constitute an important wind-launching mechanism for relativistic plasmas. In addition, the dependence of particle acceleration on imbalance could influence nonthermal electron populations in accretion disk coronae/winds and relativistic jets, thereby impacting observable emission spectra of these objects.

This work represents an important step in studying global properties of imbalanced turbulence in collisionless plasmas. It demonstrates a method for driving imbalanced turbulence in PIC simulations and develops diagnostics to study the unique aspects of imbalanced turbulence, including net motion of the plasma. Future work will refine the driving mechanism by exploring solenoidal driving and decaying turbulence set-ups to further probe the transition between perfectly imbalanced turbulence and balanced turbulence. More detailed simulations to study the impact of driving amplitude will shed light on the role of critical balance in imbalanced turbulence. Future simulations with a large number of tracked particles could measure the dependence of the energy diffusion coefficient on imbalance, thereby testing the validity of the aforementioned quasi-linear models and other test-particle MHD and PIC simulations (Teaca et al. 2014; Wong et al. 2020; Comisso & Sironi 2019). A scan of σ values (in both PIC and MHD) would help test the predicted dependence $v_{net}/v_A \sim \sigma$ of the net flow velocity on magnetization. Investigating the composition of the net flow in terms of thermal/nonthermal particles, as well as the particle momentum anisotropy, could have implications for kinetic beaming. Simulations of imbalanced turbulence in nonrelativistic and trans-relativistic electron-ion plasmas, particularly relevant to accretion flows, will also be important for understanding the fraction of energy that heats electrons. Understanding these aspects of imbalanced turbulence will aid in modeling astrophysical systems with asymmetric energy injection, such as accretion disk coronae, relativistic jets, and pulsar wind nebulae.

ACKNOWLEDGEMENTS

AMH acknowledges support from the National Science Foundation Graduate Research Fellowship Program under Grant No. DGE 1650115. VZ acknowledges support from NASA Hubble Fellowship grant HST-HF2-51426.001-A. This work was also supported by NASA ATP grants NNX17AK57 and 80NSSC20K0545, and NSF Grants AST-1806084 and AST-1903335.

This work used the Extreme Science and Engineering Discovery Environment (XSEDE), which is supported by National Science Foundation grant number ACI-1548562 (Towns et al. 2014). We used the XSEDE resources Stampede2 and Ranch at the Texas Advanced Computing Center (TACC) through allocations PHY-140041 and PHY-160032.

DATA AVAILABILITY

The simulation data underlying this article were generated at the XSEDE/TACC Stampede2 supercomputer and are archived at the TACC/Ranch storage facility. As long as the data remain in the archive, they will be shared on reasonable request to the corresponding author.

REFERENCES

- Abdo A. A., et al., 2009, *Phys. Rev. Lett.*, **102**, 181101
- Aleksić J., et al., 2015, *Journal of High Energy Astrophysics*, **5**, 30
- Alves E. P., Zrake J., Fiuza F., 2018, *Phys. Rev. Lett.*, **121**, 245101
- Balbus S. A., Hawley J. F., 1998, *Reviews of Modern Physics*, **70**, 1
- Begelman M. C., Blandford R. D., Rees M. J., 1984, *Reviews of Modern Physics*, **56**, 255
- Beresnyak A., Lazarian A., 2008, *ApJ*, **682**, 1070
- Beresnyak A., Lazarian A., 2009, *ApJ*, **702**, 460
- Beresnyak A., Lazarian A., 2010, *ApJ*, **722**, L110
- Blandford R., Eichler D., 1987, *Phys. Rep.*, **154**, 1
- Blandford R. D., Payne D. G., 1982, *MNRAS*, **199**, 883
- Boldyrev S., 2006, *Phys. Rev. Lett.*, **96**, 115002
- Boldyrev S., Perez J. C., 2009, *Phys. Rev. Lett.*, **103**, 225001
- Boldyrev S., Perez J. C., Borovsky J. E., Podesta J. J., 2011, *ApJ*, **741**, L19
- Cerutti B., Werner G. R., Uzdensky D. A., Begelman M. C., 2013, *ApJ*, **770**, 147
- Chandran B. D. G., 2000, *Phys. Rev. Lett.*, **85**, 4656
- Chandran B. D. G., 2008, *ApJ*, **685**, 646
- Chandran B. D. G., Foucart F., Tchekhovskoy A., 2018, *Journal of Plasma Physics*, **84**, 905840310
- Chen C. H. K., 2016, *Journal of Plasma Physics*, **82**, 535820602
- Chen C. H. K., Bale S. D., Salem C. S., Maruca B. A., 2013, *ApJ*, **770**, 125
- Cho J., Kim H., 2016, *Journal of Geophysical Research (Space Physics)*, **121**, 6157
- Cho J., Lazarian A., 2014, *ApJ*, **780**, 30
- Comisso L., Sironi L., 2018, *Phys. Rev. Lett.*, **121**, 255101
- Comisso L., Sironi L., 2019, *ApJ*, **886**, 122
- Cranmer S. R., van Ballegooyen A. A., Edgar R. J., 2007, *ApJS*, **171**, 520
- Davelaar J., Philippov A. A., Bromberg O., Singh C. B., 2020, *ApJ*, **896**, L31
- Demidem C., Lemoine M., Casse F., 2020, *Phys. Rev. D*, **102**, 023003
- Galtier S., Nazarenko S. V., Newell A. C., Pouquet A., 2000, *Journal of Plasma Physics*, **63**, 447
- Gogoberidze G., Voitenko Y. M., 2020, *Ap&SS*, **365**, 149
- Goldreich P., Sridhar S., 1995, *ApJ*, **438**, 763
- Grošelj D., Mallet A., Loureiro N. F., Jenko F., 2018, *Phys. Rev. Lett.*, **120**, 105101
- Hester J. J., 2008, *ARA&A*, **46**, 127
- Hoshino M., 2013, *ApJ*, **773**, 118
- Hoshino M., Lyubarsky Y., 2012, *Space Sci. Rev.*, **173**, 521
- Iroshnikov P. S., 1964, *Soviet Ast.*, **7**, 566
- Kim H., Cho J., 2015, *ApJ*, **801**, 75
- Kraichnan R. H., 1965, *Physics of Fluids*, **8**, 1385
- Kulsrud R. M., Ferrari A., 1971, *Ap&SS*, **12**, 302
- Lemoine M., 2021, arXiv e-prints, p. arXiv:2104.08199
- Lithwick Y., Goldreich P., Sridhar S., 2007, *ApJ*, **655**, 269
- Mason J., Perez J. C., Boldyrev S., Cattaneo F., 2012, *Physics of Plasmas*, **19**, 055902
- Meyer M., Horns D., Zechlin H. S., 2010, *A&A*, **523**, A2
- Meyrand R., Squire J., Schekochihin A. A., Dorland W., 2020, arXiv e-prints, p. arXiv:2009.02828
- Miloshevich G., Passot T., Sulem P. L., 2020, *ApJ*, **888**, L7
- Passot T., Sulem P. L., 2019, *Journal of Plasma Physics*, **85**, 905850301
- Perez J. C., Boldyrev S., 2009, *Phys. Rev. Lett.*, **102**, 025003
- Perez J. C., Boldyrev S., 2010a, *Physics of Plasmas*, **17**, 055903
- Perez J. C., Boldyrev S., 2010b, *ApJ*, **710**, L63
- Perez J. C., Mason J., Boldyrev S., Cattaneo F., 2012, *Physical Review X*, **2**, 041005
- Remillard R. A., McClintock J. E., 2006, *ARA&A*, **44**, 49
- Ripperda B., et al., 2021, arXiv e-prints, p. arXiv:2105.01145
- Riquelme M. A., Quataert E., Sharma P., Spitkovsky A., 2012, *ApJ*, **755**, 50
- Schekochihin A. A., 2020, arXiv e-prints, p. arXiv:2010.00699
- Schekochihin A. A., Cowley S. C., Dorland W., Hammett G. W., Howes G. G., Quataert E., Tatsuno T., 2009, *ApJS*, **182**, 310
- Schlickeiser R., 1989, *ApJ*, **336**, 243
- Shakura N. I., Sunyaev R. A., 1973, *A&A*, **500**, 33
- Sparks W. B., Biretta J. A., Macchetto F., 1996, *ApJ*, **473**, 254
- Takamoto M., Lazarian A., 2016, *ApJ*, **831**, L11
- Teaca B., Weidl M. S., Jenko F., Schlickeiser R., 2014, *Phys. Rev. E*, **90**, 021101
- TenBarge J. M., Howes G. G., Dorland W., Hammett G. W., 2014, *Computer Physics Communications*, **185**, 578
- TenBarge J. M., et al., 2021, arXiv e-prints, p. arXiv:2105.01146
- Thompson C., Blaes O., 1998, *Phys. Rev. D*, **57**, 3219
- Towns J., et al., 2014, *Computing in Science & Engineering*, **16**, 62
- Voitenko Y., De Keyser J., 2016, *ApJ*, **832**, L20
- Wang Y., Boldyrev S., Perez J. C., 2011, *ApJ*, **740**, L36
- Wong K., Zhdankin V., Uzdensky D. A., Werner G. R., Begelman M. C., 2020, *ApJ*, **893**, L7
- Zhdankin V., 2021, arXiv e-prints, p. arXiv:2106.00743
- Zhdankin V., Werner G. R., Uzdensky D. A., Begelman M. C., 2017, *Phys. Rev. Lett.*, **118**, 055103
- Zhdankin V., Uzdensky D. A., Werner G. R., Begelman M. C., 2018a, *MNRAS*, **474**, 2514
- Zhdankin V., Uzdensky D. A., Werner G. R., Begelman M. C., 2018b, *ApJ*, **867**, L18
- Zhdankin V., Uzdensky D. A., Werner G. R., Begelman M. C., 2019, *Phys. Rev. Lett.*, **122**, 055101

This paper has been typeset from a $\text{\TeX}/\text{\LaTeX}$ file prepared by the author.